Q. J. R. Meteorol. Soc. (1999), **125**, pp. 1165–1207

Kinematic characteristics of air flowing into and out of precipitating convection over the west Pacific warm pool: An airborne Doppler radar survey

By DAVID E. KINGSMILL* and ROBERT A. HOUZE Jr
University of Washington, USA

(Received 30 July 1997; revised 26 June 1998)

SUMMARY

Air flowing into and out of 25 cloud systems over the west Pacific warm pool was sampled by Doppler radars on board two NOAA WP-3D aircraft and the NCAR Electra aircraft during the Tropical Ocean/Global Atmosphere Coupled Ocean–Atmosphere Response Experiment (TOGA-COARE). In convective cells, updraught inflows and downdraught outflows tended to be positioned adjacent to each other at sharp updraught–downdraught interfaces sloping at various angles and directions. The updraught inflows were sometimes shallow and sometimes deep, often extending well above the boundary layer. Downdraught outflow magnitudes were usually stronger than updraught inflows, and the horizontal directions of the inflow and outflow were frequently offset from each other at angles of $\sim|90°|$.

In stratiform precipitation regions, the dominant airflow features were descending mid-level inflows, located at the bases of anvils and often extending into the interior of the precipitation system. These stratiform inflows originated at levels between 5 and 10 km and descended to about 3 km. A few extended down to the surface. Stratiform inflows were typically strong and sandwiched between weaker stratiform outflows at upper and lower altitudes. The stratiform-region inflow and outflow directions were frequently offset by $\sim|90°|$ in the horizontal. The mid-level inflow currents entered the stratiform regions horizontally from a direction similar to that of the large-scale ambient wind.

The mid-level stratiform inflow tended to occur in the same vertical plane as the convective downdraught outflow, although the mid-level stratiform inflow appeared to be slowed by horizontal pressure gradients before connecting with the convective downdraught outflow. In other respects, the mesoscale systems differed from a simplified two-dimensional model of airflow. The systems moved primarily by discrete propagation, and updraughts and downdraughts tended to have orthogonal horizontal relative airflow.

KEYWORDS: Radar observations TOGA-COARE Tropical convection

1. INTRODUCTION

Tropical convective clouds are a key element of the global energy balance (e.g. Riehl and Malkus 1958) and of the tropical ocean–atmosphere climate system (Webster 1994). These clouds redistribute heat, moisture and momentum throughout the atmosphere, their precipitation and downdraughts affect fluxes across the ocean–atmosphere interface, and by altering the flow fields and thermodynamic stratification within the atmosphere they affect subsequent convective activity. General circulation models and coupled ocean–atmosphere models, such as those used to represent the El-Niño/Southern Oscillation (Cane and Zebiak 1985), must parametrize all these cloud-scale processes.

To parametrize the convective momentum transport, an analogy to mixing-length theory has sometimes been applied. Schneider and Lindzen (1976) developed the concept of cumulus friction, whereby the mixing length was effectively set equal to the depth of the convection. The mass flux used in this and other similar schemes (e.g. Shapiro and Stevens 1980; Cheng and Yanai 1989) is based on one-dimensional entraining cloud models of various complexity. Implicit in all of these formulations is that the in-cloud horizontal pressure gradient is small enough to be ignored. LeMone (1983) and LeMone *et al.* (1984a) provided observational evidence that suggested this is an oversimplification. Moncrieff (1992) has tried to account for this deficiency by using an idealized dynamic model as the basis for a parametrization scheme.* The model is inspired by the pattern of the cross-line component of airflow observed in mesoscale convective systems with a leading-line/trailing-stratiform structure (e.g. Zipser 1969; Houze *et al.* 1989; Houze *et al.* 1990).

* Corresponding author, present affiliation: Atmospheric Sciences Center, Desert Research Institute, 2215 Raggio Parkway, Reno, Nevada 89512-1095, USA. e-mail: davidk@dri.edu

* Earlier versions of this model were presented in Moncrieff (1978, 1981).

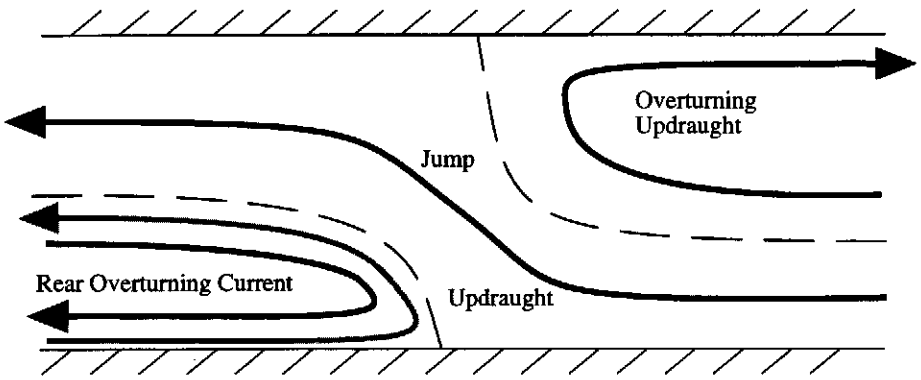

Figure 1. Schematic of the idealized flow fields used in, and adapted from, the Moncrieff (1992) dynamic model of convective momentum transport. The rear overturning current can manifest itself as a downdraught (in black) or a density current (in grey).

Specifically, the model is composed of three distinct flow branches (Fig. 1): a sloping or 'jump' updraught with front-to-rear horizontal motions; an overturning updraught located above the jump updraught with inflow originating from the front of the system; and an overturning current located below the jump updraught with inflow originating from the rear of the system. The rear overturning current can manifest itself as a downdraught (in black) or a density current (in grey). Although the mass transport properties of a downdraught and density current differ, their momentum transport properties are the same. The flow branches in this model are steady-state and two-dimensional. In some formulations they are quasi three-dimensional (Liu and Moncrieff 1996). Mathematical solutions for the heights of these flow branches, the non-hydrostatic pressure gradient across the system, as well as the mass and momentum fluxes are determined by the constraints of mass, energy and momentum conservation.

In this study, we use the Moncrieff model in Fig. 1 as a basis of comparison for dual-Doppler aircraft data showing the internal circulation patterns of mesoscale convective systems observed over the west Pacific warm pool in the Tropical Ocean/Global Atmosphere Coupled Ocean–Atmosphere Response Experiment (TOGA-COARE, Webster and Lukas 1992). This field campaign was unique in that it observed convection over a whole season in a particularly sensitive region for understanding intraseasonal and interannual variability of the atmosphere. Over this part of the earth, convection occurs over a nearly uniform warm ocean surface, away from the influences of land masses and coastlines. The tropopause is extremely high, approaching 20 km, so the convection is nearly unrestricted in the vertical. These conditions make the warm pool a natural laboratory for studying deep atmospheric convection.

In TOGA-COARE, the whole spectrum of precipitating convection over the warm pool was observed: deep, shallow, narrow and broad. The aircraft were deployed intentionally to use similar amounts of flight time observing the different classes of convection (Yuter *et al.* 1995). Flights were conducted during both active and suppressed phases of the Intraseasonal Oscillation (ISO, Madden and Julian 1972; Chen *et al.* 1996; Godfrey *et al.* 1998).

The dual-Doppler radar data obtained by the TOGA-COARE aircraft provide a unique opportunity to determine the typical characteristics of the air motions within atmospheric convection over the warm pool. The thoroughness of the four-month data sample lent statistical weight to the survey. The purpose of this paper is to use the TOGA-COARE

airborne Doppler radar data to describe and quantify the mode of mesoscale overturning of air in warm pool convection, and to compare these modes to the Moncrieff idealization of the overturning process. We accomplish this objective by focusing specifically on the properties of air flowing into (inflow) and out of (outflow) precipitating cloud systems.

2. Data

TOGA-COARE was conducted over the western Pacific warm pool region from 1 November 1992 through 28 February 1993 (Fig. 2). Our analysis of convective systems that occurred during this experiment emphasizes data collected by research aircraft but also includes satellite imagery, shipborne radar observations, balloon soundings and large-scale wind fields.

Aircraft missions were conducted on 59 days in COARE. The key aircraft for this study are three four-engine, turboprop, Doppler radar equipped aircraft comprising two National Oceanic and Atmospheric Administration (NOAA) WP-3D (hereafter P3) aircraft designated n42rf and n43rf; and the National Centre for Atmospheric Research (NCAR) Electra designated n308d. We use data from 25 days on which a mix of radar observations and flight-level wind and thermodynamic data were collected. On all but one of these days

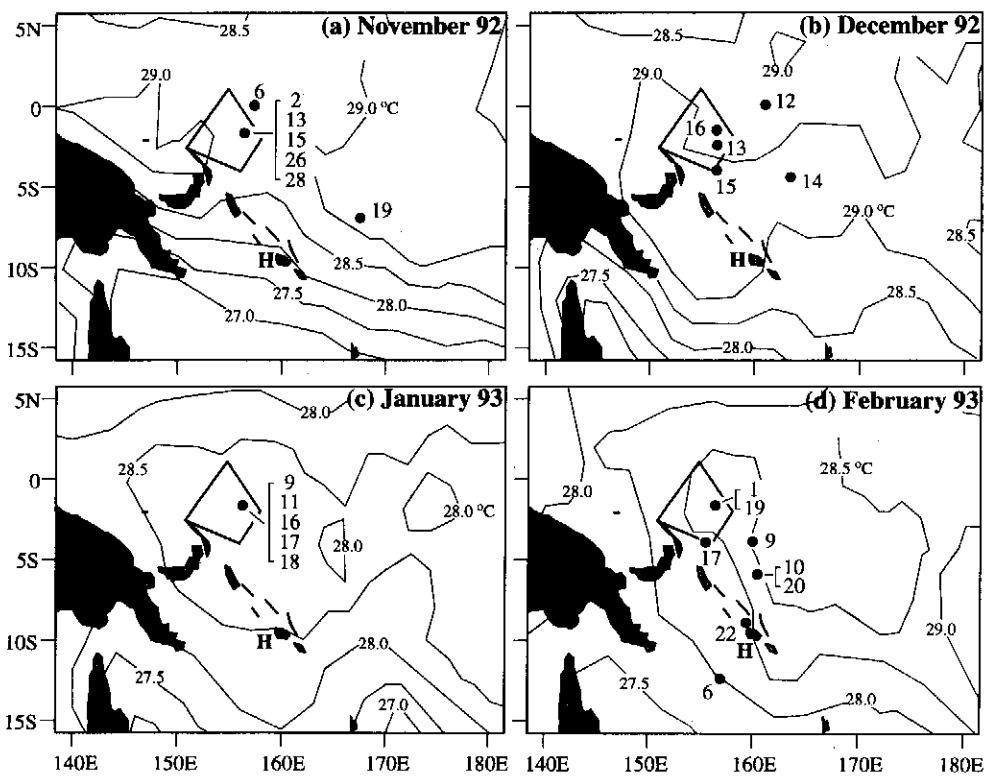

Figure 2. Maps showing the general locations of aircraft missions during the TOGA-COARE that were used for this study. Mission locations are indicated by the dots next to the days of mission commencement (see Table 1). The polygon centred near 2°S, 156°E is the Intensive Flux Array (IFA) and the 'H' near 9°S, 160°E is Honiara on Guadalcanal of the Soloman Islands, the base of operations for the NOAA P-3s and the NCAR Electra. Monthly mean sea-surface temperatures (SSTs) are plotted in each panel. (Mean SST analyses were provided by Shuyi Chen.)

TABLE 1. SUMMARY OF AIRCRAFT MISSIONS IN THIS STUDY

Mission	Date/time UTC	Aircraft
921102	2 Nov 2118–3 Nov 0551	n42rf, n43rf
921106	6 Nov 1307–6 Nov 2234	n42rf, n43rf
921113	13 Nov 2104–14 Nov 0555	n42rf, n43rf
921115	15 Nov 2150–16 Nov 0640	n43rf, n308d
921119	19 Nov 1313–19 Nov 2124	n42rf, n43rf, n308d
921126	26 Nov 2352–27 Nov 0824	n42rf, n43rf, n308d
921128	28 Nov 0150–28 Nov 0909	n42rf, n43rf, n308d
921212	12 Dec 1402–12 Dec 2329	n42rf, n43rf
921213	13 Dec 1411–13 Dec 2307	n43rf, n308d
921214	14 Dec 1301–14 Dec 2318	n42rf, n43rf, n308d
921215	15 Dec 1513–15 Dec 2306	n42rf, n43rf, n308d
921216	16 Dec 2304–17 Dec 0831	n42rf, n43rf, n308d
930109	9 Jan 2005–10 Jan 0611	n42rf, n43rf, n308d, c340
930111	11 Jan 2105–12 Jan 0430	n42rf, dc8, er2
930116	16 Jan 2105–17 Jan 0442	n42rf, n43rf, n308d, c130, c340
930117	17 Jan 2227–18 Jan 0754	n42rf, n43rf, n308d, c130, dc8, er2
930118	18 Jan 2242–19 Jan 0922	n42rf, n43rf, n308d, c130, c340, dc8, er2
930201	1 Feb 1916–2 Feb 0416	n42rf, n43rf
930206	6 Feb 1302–6 Feb 2306	n42rf, n43rf, n308d, dc8
930209	9 Feb 1318–9 Feb 2318	n42rf, n43rf, n308d
930210	10 Feb 1802–11 Feb 0252	n42rf, n43rf, n308d, dc8, c340
930217	17 Feb 1809–18 Feb 0307	n42rf, n308d, dc8
930219	19 Feb 1905–20 Feb 0351	n43rf
930220	20 Feb 1834–21 Feb 0412	n42rf, n43rf, dc8, er2
930222	22 Feb 1800–23 Feb 0243	n42rf, n43rf, dc8, er2

Participating aircraft are denoted as follows: n42rf (NOAA P-3 N42RF); n43rf (NOAA P-3 N43RF); n308d (NCAR ELECTRA); dc8 (NASA DC8); er2 (NASA ER2); c340 (Flinders University CESSNA); and c130 (UK Meteorological Office C130).

the data were collected by two or more of these aircraft flying in a co-ordinated pattern to optimize the wind, thermodynamic and radar data (Table 1; Fig. 2).

Radar systems on the aircraft sense precipitation remotely (Table 2). Each P3 aircraft has a radar antenna located on the underside of its fuselage. This lower fuselage (LF) radar surveys a quasi-horizontal plane, and produces a reflectivity field that indicates the relative intensity of precipitation over distances up to 100–200 km. Although its vertical beam width is large, the LF radar provides a broad context for the horizontal precipitation structure with good horizontal resolution. A Doppler radar with an antenna on the tail of each of the three aircraft scanned a quasi-vertical plane and measured both reflectivity and radial velocity. The tail Doppler radar has very high spatial resolution. Its radial resolution is 75–150 m, and its beam is 250–1000 m wide for targets within 40 km of the aircraft. The tail Doppler radar alternates between scanning ~20° fore and aft of the plane orthogonal to the aircraft's ground track. Since the aircraft moves rapidly, the beams of the fore and aft scans intersect at 40°–45° angles and are temporally offset from each other by ~1 min for each 10 km distance from the aircraft. The radial-velocity information from these intersecting scans can be combined to synthesize three-dimensional wind fields using Fore–Aft Scanning Technique (FAST) dual-Doppler methodology of Jorgensen *et al.* (1996).

Our analysis takes a comprehensive, statistical approach to the TOGA-COARE airborne radar data. The *entire* radar dataset was perused for each of the 25 selected missions (Table 1). To obtain the horizontal mesoscale context, the LF radar data were examined at intervals of 10–30 min using NCAR's Zebra software (Corbet *et al.* 1994) and TOGA-COARE aircraft mission summaries (Yuter *et al.* 1995). The high-resolution quasi-vertical

TABLE 2. CHARACTERISTICS OF THE RADARS USED IN THIS STUDY

	NOAA P-3 Lower Fuselage Radar C-band	NOAA P-3 Tail Doppler Radar X-band	NCAR ELDORA Tail Doppler Radar X-band
Wavelength (cm)	5.59	3.22	3.2
Peak Transmitted Power (kW)	70	60	35–50
Beam width (deg)			
horizontal	1.1	1.35	1.8
vertical	4.1	1.9	1.8
Gate spacing (m)	900	75, 150, 300	150
Antennae Rotation Rate (deg/s)	6	60	66
Pulse Repetition Frequency (Hz)	200	1600	2000
Unambiguous Velocity (m/s)	NA	12.88	16
Polarization	horizontal	vertical (n42RF) horizontal (n43RF)	horizontal

cross-sections from the tail Doppler radar received more detailed attention. They were perused in an uninterpolated form (i.e. at full spatial resolution) at sampling intervals ranging from 10 to 180 seconds using NCAR Research Data Support System software (RDDSS) (Oye and Carbone 1981). For selected time periods (156 in all), the fore and aft scans were combined to synthesize three-dimensional wind fields to aid in the interpretation of the single-Doppler data. After using RDSS to unfold aliased radial velocities into their proper Nyquist interval, the data were interpolated (Cressman 1959; Oye *et al.* 1995) to one of two Cartesian grids, dependent upon the radar scanning strategy. If the radar scanned on both sides of the aircraft, a $1.5 \times 1.5 \times 0.8$ km grid was used. However, if the radar scanned on just one side of the aircraft a $0.75 \times 0.75 \times 0.8$ km grid was used, to take advantage of the higher sampling rate in the direction of the aircraft ground track. After interpolation, three-dimensional wind fields were synthesized using the FAST dual-Doppler methodology in the NCAR CEDRIC* software package (Mohr *et al.* 1986). Because of the uncertainties in determining vertical velocities using the FAST methodology we emphasized use of the horizontal wind fields and did not draw any conclusions that depend on the vertical velocity fields.

Large-scale wind information was obtained from analyses generated by the National Centers for Environmental Prediction (NCEP). These analyses were available every 12 hours with 2.5° horizontal resolution at the 1000, 925, 850, 700, 500, 400, 300, 250, 200, 150 and 100 mb constant pressure levels. Parameters used in the subsequent discussion are listed in the appendix.

3. PRECIPITATION STRUCTURE

The airborne radar observations of COARE convective clouds revealed precipitation structures generally similar to those seen over the tropical Atlantic in GATE (Global Atmospheric Research Program Atlantic Tropical Experiment) convective systems (Houze and Betts 1981). The primary mesoscale cloud systems over the tropical oceans appear in satellite imagery as regions of very cold cloud top. These cold cloud top areas are often

* Custom Editing and Display of Reduced Information in Cartesian space.

loosely referred to as mesoscale convective systems (MCSs) or cloud clusters (Martin and Schreiner 1981; Williams and House 1987; Mapes and Houze 1993; Chen *et al.* 1996). Shipborne radar observations in GATE typically showed one or more distinct mesoscale precipitation features (MPFs) under a region of cold cloud top. An MPF is a constituent mesoscale element of an MCS. Leary and Houze (1979) presented a conceptual model for the life cycle of an MPF. In its 'formative stage' (F), an MPF is a group or line of isolated, relatively shallow cumulonimbus. As the MPF evolves into its 'intensifying stage' (I), the depth of convection increases with new cells forming between and on the low-level inflow side of existing cells. The old and new cells merge to form one connected region of precipitation. During the 'mature stage' (M) of the MPF, a region of actively growing deep convection is adjacent to a large area of more horizontally uniform precipitation which contains older cells at various stages of decay and exhibits a distinct maximum of reflectivity at the melting level. Finally, as the MPF enters its 'dissipating stage' (D) new convective cells weaken and form less frequently, and the precipitation pattern becomes more horizontally uniform. We find that this conceptual model applies both to those systems that attain large horizontal and vertical extents and to those that never organize and grow into contiguous mesoscale rain areas. Leary and Houze (1979) pointed out that the life cycle can be truncated at any stage (because of unfavourable environmental conditions, merger with another MPF, etc.). Thus, only the most favoured systems go through the complete cycle.

There are limits to which we can judge the COARE aircraft data in comparison to the Leary and Houze (1979) conceptual model, since the duration of an aircraft mission was often not long enough to sample all four stages of an MPF. As Table 3 indicates, usually 1 to 2 of the 4 stages were observed. During active phases of the ISO, convective clouds were abundant in all stages of development. Some of these developed into deep convective systems, but many did not. There was a tendency to sample the M stages of the more horizontally and vertically extensive MPFs. As a result, aircraft data in the F or I stages of MPFs were collected mostly during suppressed phases of the ISO, when large-scale conditions apparently did not favour full convective development according to the Leary and Houze life cycle. These MPFs did not mature into broad, contiguous mesoscale precipitation areas.

Even with these sampling limitations, important aspects of system development could be assessed since convective cells continue to form, grow and decay throughout the M stage of an MPF, and the aircraft would often focus on a region of new cell development and monitor the evolution of the cellular region of an MPF until it blended into the region of more uniform precipitation left by previous cells.

Convection observed by aircraft in COARE exhibited a predominantly discrete mode of propagation. Houze (1993) describes this archetype as an unsteady succession of convective cells that grow at discrete horizontal intervals with respect to each other and evolve into one uniform stratiform precipitation region. Mapes and Houze (1992) observed several of these types of systems in the Australian monsoon. Continuously propagating, quasi-steady-state 'squall lines', consistent with the leading-line/trailing-stratiform conceptual model of mesoscale convective systems (Houze *et al.* 1989, 1990) were relatively rare. Jorgensen *et al.* (1997) have used aircraft data to describe one well documented continuously propagating system that occurred during COARE. Our perusal of all the radar data from the research vessels* *Xiang Yang Hong* and *John V. Vickers* (see Short *et al.* 1997 for a description of the location and operating characteristics of these radars during

* The three-dimensional volumes of ship radar reflectivity and Doppler radial velocities have been interpolated at 1-hour intervals and viewed three dimensionally in Zebra. The low-level elevation scans have been viewed in Zebra at higher time resolution.

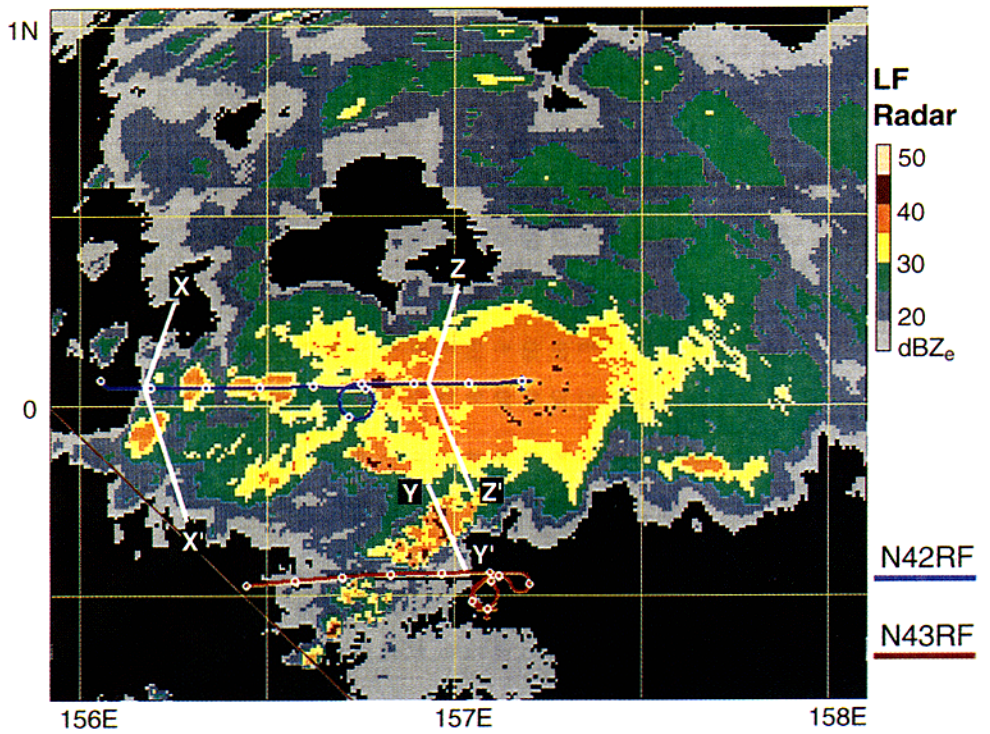

Figure 3. Lower-fuselage radar reflectivity on 6 November 1992 at about 1718 UTC. The colour key indicates values of reflectivity in dBZ_e. Line segments X–X′, Y–Y′ and Z–Z′ refer to tail radar cross-sections shown in Fig. 4. The latitude and longitude grid is at 0.5° intervals.

TOGA-COARE) also suggests that discretely propagating systems were more common than continuously propagating systems.

Figures 3 and 4 show an example of a discretely propagating system, which occurred on 6 November 1992 (MPF 921106, Table 3). The south-western portion of the system contained developing convection, evident from the small-scale, 35–45 dBZ_e maxima in reflectivity (Fig. 3, south of the equator, 156–157°E). Vertical cross-sections in Fig. 4(a) and (b) show cell tops as high as 15 km, providing further evidence of the vigorous convective nature of the precipitation in this area. The centre region of reflectivity in Fig. 3 (3°N–2°S, 156.7–158°E) is somewhat older than the convection to the south and west and has a more uniform horizontal precipitation pattern. A well-defined radar 'bright-band' (Battan 1973) just below the 5 km level indicated the stratiform nature of the precipitation in the region (Fig. 4(c)). Embedded maxima in reflectivity extending below and above the bright band were typical of such stratiform regions. They appear to be the signature of decaying convection. The northern and eastern portions of the system are oldest and have the lowest and most uniform values of reflectivity (Fig. 3). The precipitation area in this system expanded by discrete jumps, with new development occurring systematically on the southern and western edges of active convection.

From the 25 aircraft missions, 33 separate MPFs were identified. The boundaries between MPFs observed on a single mission were based subjectively upon their spatial and temporal continuity. Of all the MPFs observed by the aircraft, 23 exhibited discretely propagating characteristics, two exhibited continuously propagating characteristics, and six exhibited combinations of both (Table 3).

TABLE 3. CHARACTERISTICS OF MPFs DETERMINED FROM THE AIRBORNE RADAR DATA

MPF	STAGE	CAT	ISO	MAX AREA (km^2)	MAX Z_{TOP} (km)	PROP	$\lvert V_{PROP} \rvert$ ($m\ s^{-1}$)	DIR V_{PROP} (from, deg)	LSWIND ($m\ s^{-1}$, deg) At the following pressure levels in mb											
									1000		850		700		500		400		200	
921102A	I	DN	A	80 × 20	15	D	4	315	2	225	2	225	8	225	3	225	3	225	15	90
921106A	M	DB	A	>300 × 180	17	D	8	270	4	225	4	225	3	225	4	135	3	135	11	90
921113A	F	S	S	40 × 10	7	D	3	90	3	135	6	135	3	180	3	45	6	45	10	45
921115A	F	S*	S	10 × 10	no data	D	8	225	5	225	4	180	5	270	2	45	4	45	14	45
921119A	M	DB	S	>300 × 120	16	D	6	135	6	135	5	135	3	135	3	225	5	180	8	45
921126A	D	DN	S	150 × 120	12	NA	NA	NA	3	225	4	225	5	90	10	90	10	90	13	45
921126B	I	DN	S	120 × 60	16	D	3	180	3	225	4	225	5	90	10	90	10	90	13	45
921128A	F	S	S	10 × 10	5	D	4	315	3	225	3	90	4	90	5	90	6	90	7	135
921212A	M	DB	A	310 × 160	18	D	3	135	2	315	2	0	4	0	10	45	9	45	7	45
921213A	M, D	DB	A	>540 × 300	19	D	10	0	5	315	5	315	5	0	9	90	8	90	8	90
921214A	M	DB	A	260 × 160	16	D	7	225	5	270	6	270	6	270	6	45	8	45	4	225
921214B	M	DB	A	>260 × 140	19	D	6	270	5	270	6	270	6	270	6	45	8	45	4	225
921214C	M	DB	A	>240 × 150	18	D	10	270	5	270	6	270	6	270	6	45	8	45	4	225
921215A	M	DB	A	>520 × >250	20	D	7	225	2	225	5	270	5	270	4	90	4	90	3	90
921216A	I	DN	A	90 × 40	15	D	7	225	3	225	4	225	2	225	9	45	6	45	4	135
930109A	I	DN	S	200 × 30	14	D, C	6	315	2	0	2	90	4	180	3	225	4	225	7	90
930111A	F	S	S*	30 × 10	6	D	4	45	2	90	2	90	2	135	2	45	6	45	10	45
930116A	I	DN	S	140 × 30	16	D	9	90	4	90	5	90	6	90	7	45	4	45	11	270
930117A	I	DN	U/A	330 × 70	13	D, C	4	45	3	90	4	90	5	90	5	90	4	45	8	270
930118A	I	DN	U/A	60 × 20	12	D	2	180	4	90	6	90	8	90	7	90	8	45	7	315

TABLE 3. CONTINUED

MPF	STAGE	CAT	ISO	MAX AREA (km^2)	MAX Z_{TOP} (km)	PROP	$\lvert V_{PROP} \rvert$ ($m\ s^{-1}$)	DIR V_{PROP} (from, deg)	LSWIND ($m\ s^{-1}$, deg) At the following pressure levels in mb											
									1000		850		700		500		400		200	
930118B	I, M	DB	U/A	300 × 150	15	D	5	135	4	90	6	90	8	90	7	90	8	45	7	315
930201A	F	S	U/A	30 × 10	4	D, C	11	315	5	315	8	315	11	270	6	270	2	270	15	90
930206A	M, D	DB	A	>400 × 120	17	D	5	315	5	0	9	315	12	270	10	270	9	315	3	270
930206B	I	DN	A	70 × 20	15	C, D	8	315	5	0	9	315	12	270	10	270	9	315	3	270
930206C	I, M	DB	A	>280 × 120	16	D, C	10	315	5	0	9	315	12	270	10	270	9	315	3	270
930209A	M	DB	A	290 × 180	16	D	6	225	5	270	8	270	7	225	5	135	5	90	13	90
930209B	I, M, D	DB	A	>310 × 140	19	D	7	225	5	270	8	270	7	225	5	135	5	90	13	90
930210A	M, D	DB	A	>390 × 150	17	D	7	225	6	270	10	225	11	225	4	135	4	45	5	45
930210B	I, M	DB	A	>270 × 150	16	C	12	180	6	270	10	225	11	225	4	135	4	45	5	45
930217A	I	DN	A	180 × 50	15	D	5	315	4	315	4	315	3	0	2	0	2	0	7	90
930219A	F	S	A	no echo	no echo	no echo	—	—	5	315	8	315	7	315	5	315	3	45	6	90
930220A	M, D	DB	A	350 × 180	18	D, C	10	270	7	270	11	270	12	270	9	225	4	180	11	135
930222A	M, D	DB	A	>500 × >200	19	C	11	270	8	315	14	270	14	270	10	270	7	225	13	135

The parameters are: STAGE, the evolutionary stage of development during aircraft sampling based on the Leary and Houze (1979) conceptual model (F, formative; I, intensifying; M, mature; D, dissipating); CAT, the size category of the convection sampled by the aircraft as defined in Kingsmill and Houze (1999; S, shallow; DN, deep narrow; DB, deep broad); ISO, the phase of the ISO based upon Chen *et al.* (1996; A, active; S, suppressed; U, unclassified); AREA, the horizontal area of the MPF as based on the lower fuselage radar; Z_{TOP}, the echo top based upon the tail radar; PROP, the mode of propagation (D, discrete; C, continuous); V_{PROP}, the mean propagation speed and direction of distinct echo features; and LSWIND, the NCEP large-scale wind speed and direction at 1000, 850, 700, 500, 400 and 200 mb. The AREA entries accompanied by '>' refer to areal extents at least as large as indicated.

Due to the lack of tail radar data, the CAT entry for 921115A was defined as shallow, based upon the exceptionally small horizontal area of the echoes. Due to the lack of satellite data, the ISO entry for 930111A was defined as suppressed, based upon the conditions immediately before and after this time period. These values are marked with asterisks.

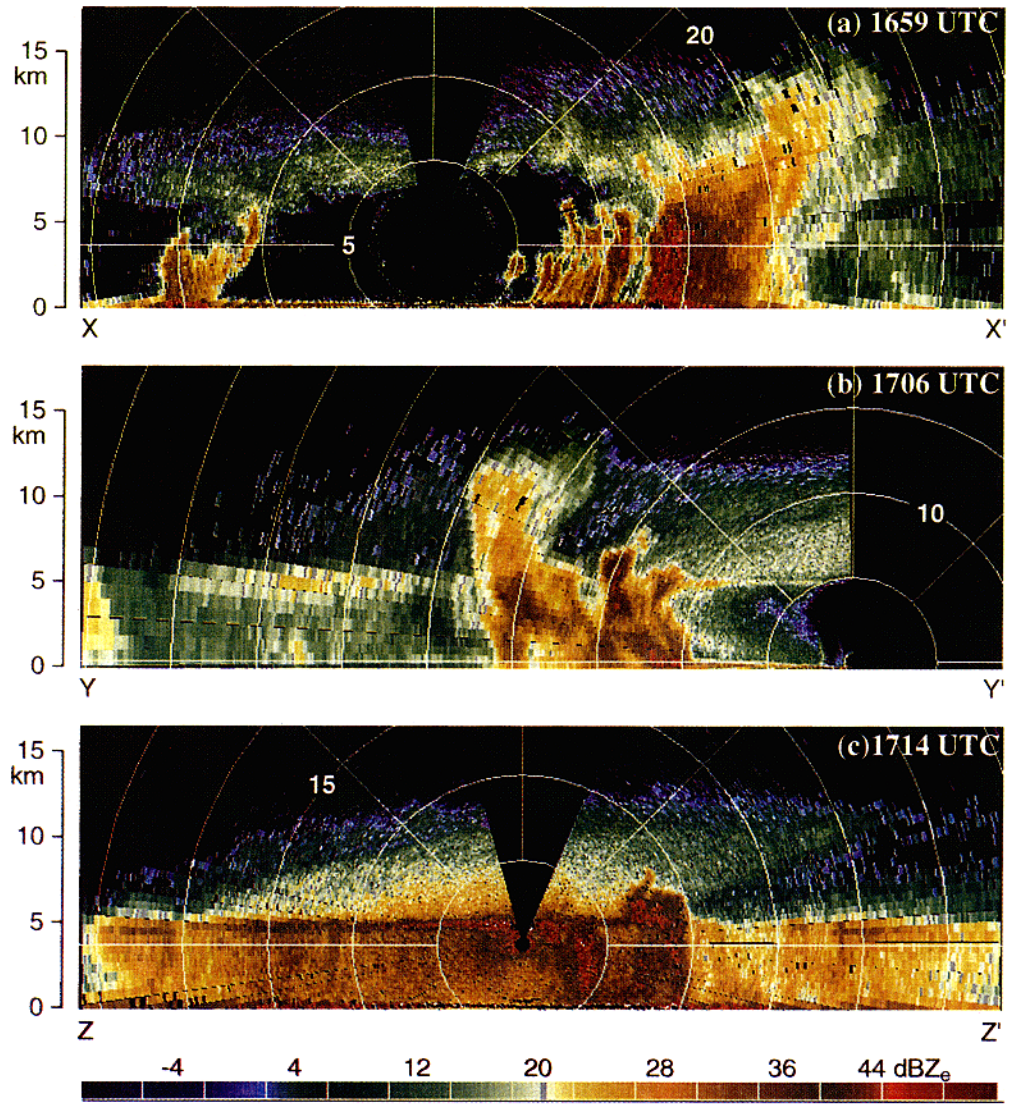

Figure 4. Tail radar reflectivity on 6 November 1992. (a) n42rf cross-section X–X′ at 1659.26 UTC. (b) n43rf cross-section Y–Y′ at 1706.57 UTC and (c) n42rf cross-section Z–Z′ at 1714.22 UTC. The colour key indicates the reflectivity values. The radar is located at the centre of the range–azimuth grids. Range rings are at 5 km intervals. Locations of cross-sections with respect to the horizontal precipitation pattern are indicated in Fig. 3. See text and Table 1 for aircraft designations.

The speed and direction of propagation of the convection within these MPFs were determined by calculating mean values of the motion of distinct cellular features observed by the LF radar over a period of at least 15 min. Individual cell motion vectors are estimated to be accurate within ± 2 m s^{-1} of magnitude and $\pm 20°$ of direction. This motion should not be confused with the mesoscale system motion which requires more subjective interpretation and is therefore subject to greater error, especially with the relatively disorganized, discretely propagating systems that are most common in COARE. A wide variety of individual cell motion vectors often occurred within a single MPF, especially

those MPFs exhibiting discretely propagating characteristics. Propagation speeds ($|\mathbf{V}_{PROP}|$) were primarily less than 10 m s^{-1}, and directions, while broadly distributed, showed a tendency for a component of movement from west to east, especially during active periods of the ISO. The propagation vectors were related to the large-scale winds in the lowest 300 mb with the best correlation in the 850–700 mb layer. This result is illustrated in Fig. 5, which shows polar histograms of the directional difference between large-scale wind direction and propagation direction, as well as polar scatterplots of the ratio between large-scale wind speed and propagation speed. In the polar histograms (Fig. 5(a) to (d), positive (negative) values of the directional difference indicate that the directions of $\mathbf{V}_{PROP}$ are rotated counter-clockwise (clockwise) relative to the large-scale wind direction. At 850 and 700 mb, the histograms show distinct peaks in directional difference at 0°, while at 1000 mb the peak is at 45° but with nearly as high a frequency at 0°. However, at 500 mb the peaks in directional difference are between −45° and −90°. In the polar scatterplots (Fig. 5(e) to (h)), points outside (inside) the unit circle indicate that $|\mathbf{V}_{PROP}|$ is less (greater) than the large-scale wind speed. At 1000 mb, the scatterplot shows that the propagation speed was primarily greater than the large-scale wind speed. Above this level there is more scatter, with points on both sides of the unit circle. The points along the 0° directional difference radial at 850 and 700 mb (i.e. the peak directional difference at those levels) lie between a magnitude ratio of 0.5 to 2.0. It appears that cell propagation is not as well correlated with large-scale wind speed as it is with large-scale wind direction. The tendency of the propagation speed to exceed the ambient wind speed at 1000 mb suggests that the convective downdraughts systematically transported momentum downward.

4. Air motions in convective cells

The dominant kinematic structures in convective cells were the inflows and outflows associated with updraughts and downdraughts. Such structures were imagined and conceptualized in early studies, prior to extensive radar and satellite observations (e.g. Newton 1963; Ludlam 1963). They are also seen in convective and mesoscale models (e.g. Thorpe *et al.* 1982; Rotunno *et al.* 1988; and many others). Although it is difficult to diagnose vertical velocities quantitatively from the COARE airborne dual-Doppler radar data (section 2), it is easy to identify the signatures of updraughts and downdraughts in the patterns of single-Doppler raw radial velocity (VR) associated with convective cells. Updraughts are characterized by well-defined channels of VR rising out of the boundary layer and sloping upward into a cell, usually with the same sense of slope as the core of reflectivity with which each is associated. The tail Doppler radar data presented in Fig. 6 provides an example. On the right side of the radar, located at the centre of the range–elevation angle grid, the updraught inflow is associated with the deep, blue-green channel of negative VR sloping upward from the surface in the same sense as the reflectivity core. At increasing altitudes, updraught inflows generally become less distinct. However, near the tops of convective cells, divergent updraught outflow signatures are often evident. In Fig. 6(b), this feature is associated with both the red maximum of positive VR at 15 km altitude on the front side of the reflectivity cell, and the dark blue minimum of negative VR on the back side of the cell at nearly the same altitude. Note that at large elevation angles, especially above 45° or below −45°, caution must be exercised in relating VR structures to horizontal flow structures, since vertical motions may contribute significantly to VR at these locations. The bold lines in Fig. 6 along the ±45° elevation angle radials are meant to highlight this fact. The downdraught signature is equally distinct. It is a region of VR opposite in sign to the VR of the updraught inflow. It lies just below the updraught inflow such that the two airflow features are separated by a sharp gradient of VR. The downward sloping

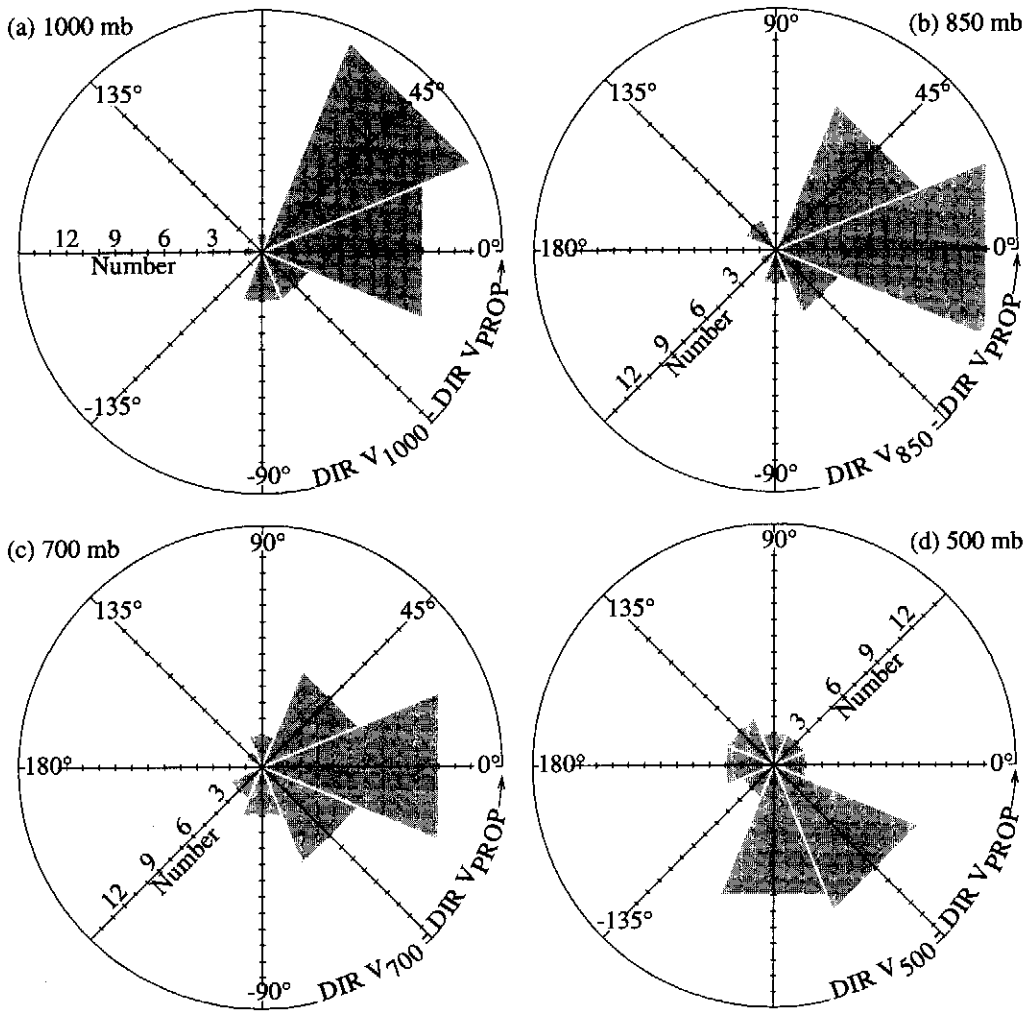

Figure 5. Comparison of NCEP large-scale winds versus cell propagation (V_{PROP}) in an earth-relative sense. Polar histograms of the directional difference between earth-relative large-scale wind direction and earth-relative cell propagation direction at (a) 1000, (b) 850, (c) 700 and (d) 500 mb. Polar scatterplots of the ratio between earth-relative large-scale wind speed and earth-relative cell propagation speed as a function of directional difference at (e) 1000, (f) 850, (g) 700 and (h) 500 mb. Data points are subdivided by month as indicated in the figure; the grey arrow represents a reference vector of unit length.

brown-red channel of positive VR in Fig. 6 is an example of one of these downdraught outflows. The downstream edge of the downdraught air slopes down to the surface in a manner that resembles a density current (Simpson 1987). However, it is not clear that this analogy is exact. The tail radar was often unable to obtain meaningful data in the lowest 500 m and was insensitive to scatterers in the clear air. Therefore, shallow density currents emanating from the observed downdraught outflows might have escaped detection. Nonetheless, cross-sections such as Fig. 6 suggest that the denser downdraught outflow slides under the sloping updraught channel, and appears to be the primary mechanism in bringing the low-level air above its level of free convection. The updraught–downdraught interface thus appears to be a nearly zero-order discontinuous boundary between the up-

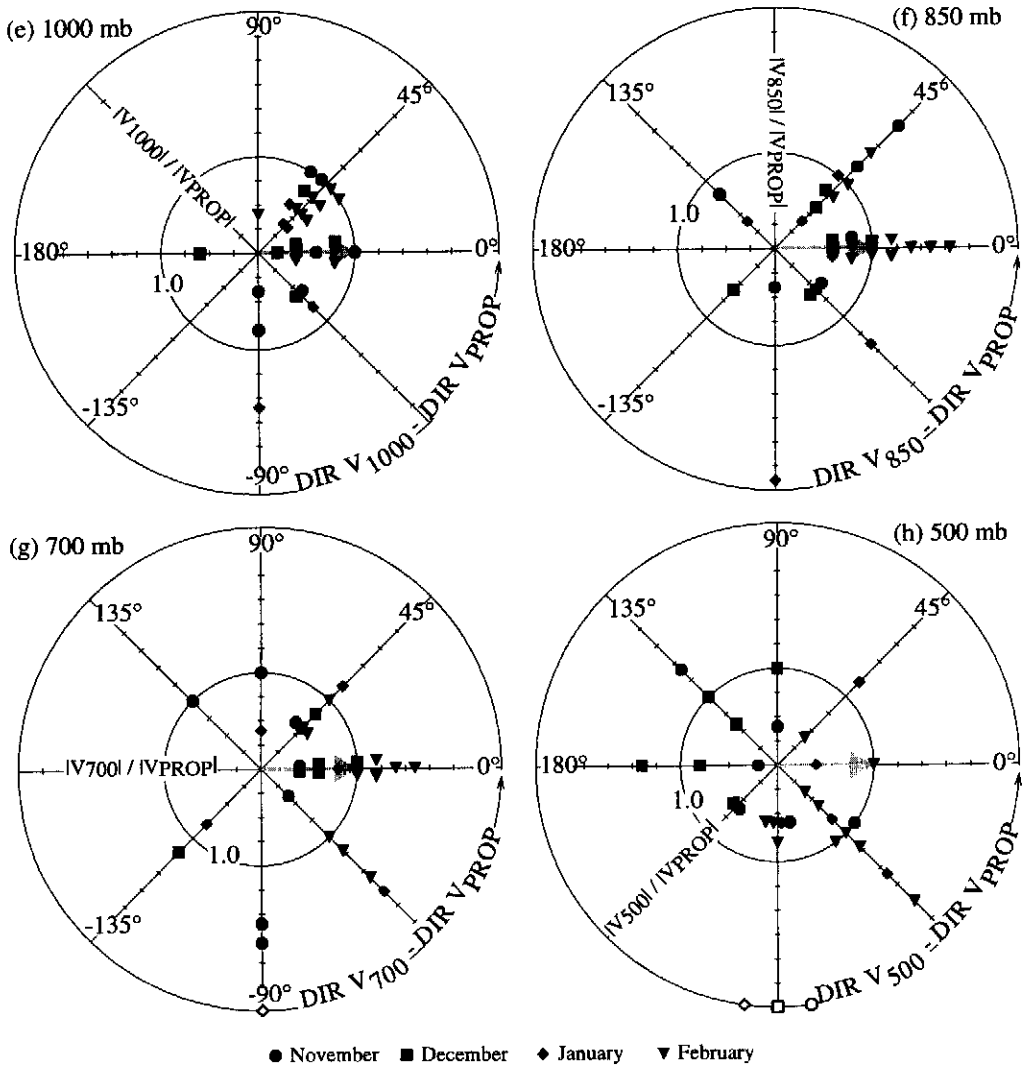

Figure 5. Continued.

ward and downward branches of a convective mesoscale thermally direct circulation. FAST dual-Doppler syntheses of the tail radar data confirm that convergence is concentrated at the boundary of the updraught and downdraught channels, and vertical velocity patterns computed from the divergence field show upward motion in the expected sense above the boundary. Figure 7 provides an example of these fields for the same vertical cross-section as shown in Fig. 6. The dual-Doppler winds corresponding to the cross-section in Fig. 6 exhibit the divergence and vertical velocity fields shown in Fig. 7. These fields confirm that convergence occurred along the sloping boundary of updraught inflow and downdraught outflow and that the inflow current inferred from the radial velocity pattern in Fig. 6 was indeed rising, i.e. it was an *updraught* current. Similarly the perceived outflow current was subsiding in the manner of a thermally direct circulation. Many other dual-Doppler syntheses from the COARE aircraft data show similar patterns in relation to the radial velocity data.

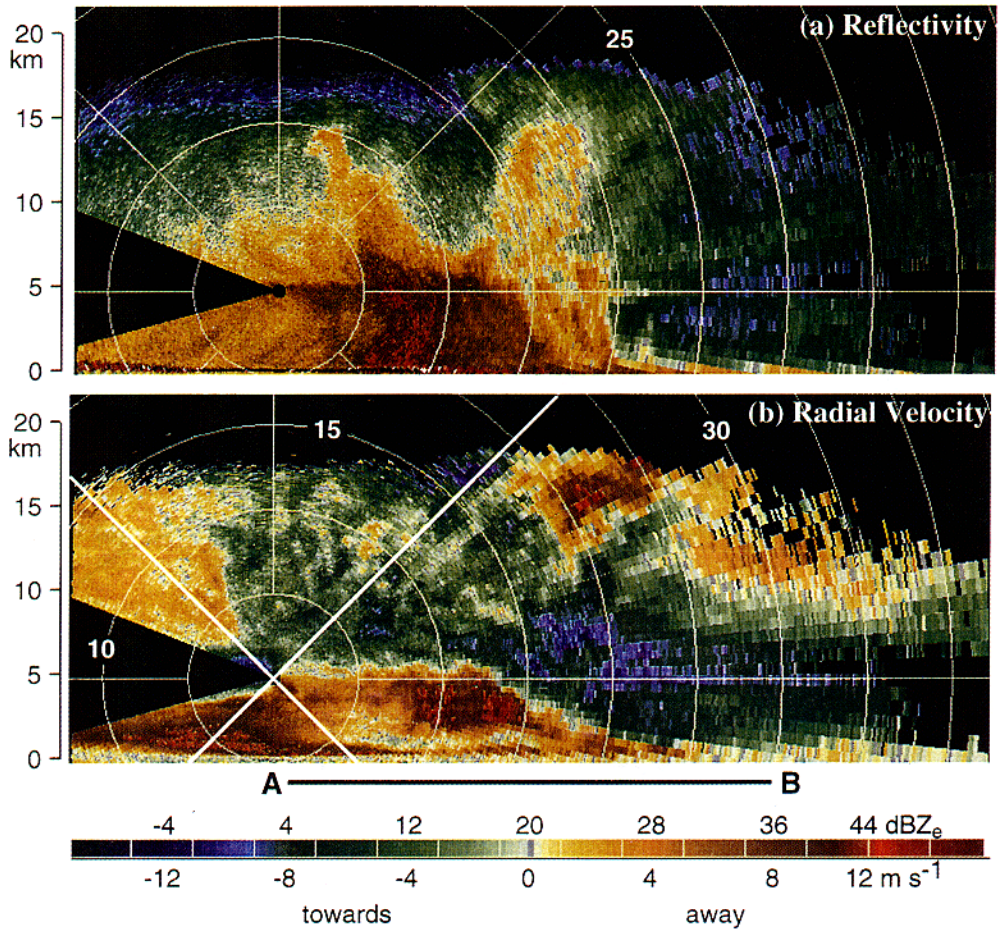

Figure 6. Tail radar vertical cross-sections of (a) reflectivity and (b) radial velocity on 14 December 1992 at 1630.04 UTC. The colour key indicates reflectivity and radial velocity values. Positive (negative) values of radial velocity are directed away from (towards) the radar. The radar is located at the centre of the range–azimuth grid. Range rings are at 5 km intervals. The line segment AB represents the dual-Doppler vertical cross-section shown in Fig. 7. The bold lines in (b) indicate 45°. See text for further details.

We examined all of the tail Doppler radar data from the 25 aircraft missions to locate the signatures of convective updraught inflows and downdraught outflows in displays similar to those in Fig. 6 (~27 000 cross-sections viewed in all); where the data allowed, we confirmed our inferences by comparing with dual-Doppler cross-sections like those in Fig. 7. Although we did not keep an exact count, we have used 156 dual-Doppler volumes from flights on 25 different days to make hundreds of comparisons of single and dual-Doppler cross-sections like the ones in Figs. 6 and 7, and the comparisons were seldom less convincing than this example. The results of this comprehensive examination generally characterize the airflow into and out of the convective updraughts and downdraughts of warm-pool convection. To tabulate the results of this extensive analysis systematically and quantitatively, we devised a simplified conceptual model of the convective updraught and downdraught structures (Fig. 8). The parameters defined in the model indicate both the geometry and strength of the updraught and downdraught patterns recognizable in tail radar cross-sections. A list containing the definitions of these parameters is in the appendix.

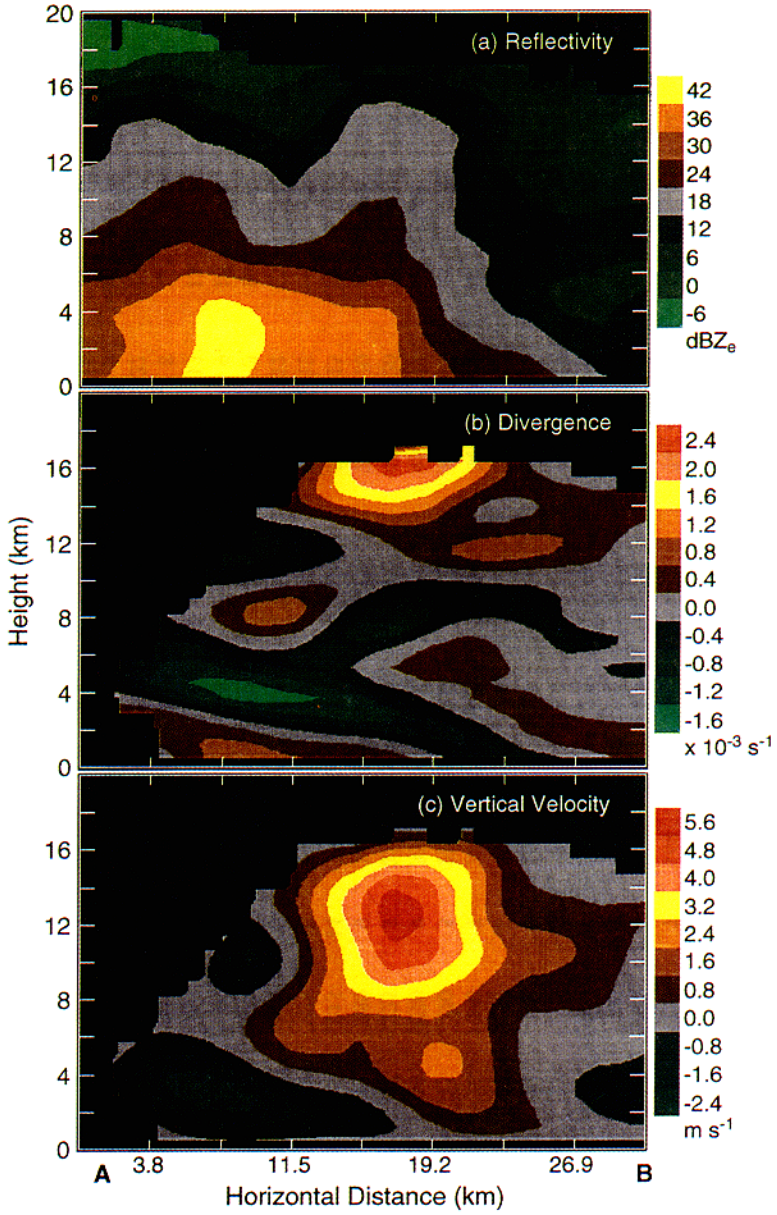

Figure 7. Dual-Doppler-derived vertical cross-sections of (a) tail radar reflectivity, (b) divergence and (c) vertical velocity on 14 December 1992 at 1630 UTC along the line segment AB shown in Fig. 6. The colour keys indicate reflectivity, divergence and vertical-velocity values respectively.

By inspection of the tail radar cross-sections, such as in Fig. 6, and the associated dual-Doppler wind field analyses, we determined and recorded the values of all the parameters defined in Fig. 8 for 27 distinct updraught–downdraught pairs observed by the tail Doppler radars (Table 4). Since it was often difficult to draw a clear distinction between different convective cells in an MPF based solely upon reflectivity structure, the spatial continuity of the updraught–downdraught patterns as well as the spatial continuity of the directions associated with these airflows were used as the primary criteria in subjectively distinguishing

TABLE 4. CHARACTERISTICS OF AIRFLOW PARAMETERS ASSOCIATED WITH CONVECTIVE CELLS

CASE	Earth-relative MAX $\lvert V_{E_{UI}}\rvert$ ($m\ s^{-1}$)	Earth-relative DIR $V_{E_{UI}}$ (deg)	Cell-relative MAX $\lvert V_{C_{UI}}\rvert$ ($m\ s^{-1}$)	Cell-relative DIR $V_{C_{UI}}$ (deg)	Earth-relative MAX $\lvert V_{E_{DO}}\rvert$ ($m\ s^{-1}$)	Earth-relative DIR $V_{E_{DO}}$ (deg)	Cell-relative MAX $\lvert V_{C_{DO}}\rvert$ ($m\ s^{-1}$)	Cell-relative DIR $V_{C_{DO}}$ (deg)	OBS. $Z_{E_{UI}}$ (km)	EST $Z_{C_{UI}}$ ($m\ s^{-1}$)	MAX $\Delta VR\lvert_{\Delta r=5\ km}$ ($m\ s^{-1}$)	MAX $SLOPE_{UI}$ (deg)	MAX VR_{FUO} ($m\ s^{-1}$)	MAX VR_{RUO} ($m\ s^{-1}$)	ΔX_{UO} (km)	α_{UO} (deg)	MAX Z_{TOP} (km)
921102A I*	5	225	7	184	9	315	5	315	2.0	2.8	−13	56	13	14	5	33	16
921106A I*	4	270	4	90	9	225	7	168	3.0	NA	−13	76	8	11	4	34	17
921106A II*	8	180	11	136	8	225	6	160	1.0	1.5	−11	34	5	11	5	35	13
921119A I*	6	225	9	271	10	90	7	52	4.0	7.1	−14	34	10	13	12	34	14
921126B I	6	0	9	0	13	225	11	237	2.0	2.5	−13	45	4	7	5	27	14
921212A I*	5	270	8	288	13	45	13	30	3.0	3.8	−17	74	24	18	12	42	18
921213A I*	6	270	11	211	13	315	9	266	3.0	11.8	−16	45	26	10	11	41	19
921214B I*	12	270	6	270	12	90	18	90	9.0	6.8	−22	34	15	13	7	53	19
921214B II*	5	45	10	70	13	270	7	270	4.0	7.9	−16	34	13	14	6	35	19
921214C I*	7	315	7	46	15	270	5	270	2.0	19.0	−15	45	12	12	9	20	19
921215A I	15	225	8	225	13	270	9	303	8.0	5.8	−17	45	12	22	13	26	19
921215A II	10	315	12	351	12	225	5	225	7.0	8.7	−17	45	20	16	11	33	20
921215A III	6	225	1	45	12	180	9	143	5.0	NA	−15	72	10	16	5	32	20
921215A IV	10	225	3	225	12	315	14	346	3.0	1.9	−20	56	15	12	5	58	19
930109A I	7	315	1	315	8	225	10	190	2.0	1.1	−13	72	12	8	5	49	14
930116A I	9	45	7	341	7	135	6	216	5.0	6.6	−12	37	12	13	6	26	17
930118B I*	6	90	4	42	10	135	5	135	1.0	1.0	−14	45	3	16	6	28	15
930118B II*	7	135	2	135	13	90	10	72	1.0	0.6	−16	63	9	10	4	55	15
930206A I	10	0	7	28	15	315	10	315	1.0	1.0	−20	56	13	13	4	56	17
930209A I*	11	315	12	343	13	225	7	225	1.0	1.0	−12	53	8	13	5	22	17
930209B I*	6	315	9	6	20	225	13	225	1.0	5.0	−16	72	22	19	10	30	20
930210A I*	9	225	2	225	16	315	17	337	4.0	2.5	−13	56	2	15	3	54	17
930210B I*	9	315	20	341	18	225	13	268	2.0	8.9	−19	32	18	15	7	45	17
930217A I	10	315	5	315	12	225	13	204	4.0	3.1	−12	56	8	13	7	23	13
930220A I*	9	270	1	90	12	225	9	171	4.0	NA	−14	76	16	13	8	37	19
930220A II*	10	270	0	270	16	315	11	352	1.0	0.6	−16	63	5	13	4	58	17
930222A I	9	315	8	33	19	270	8	270	1.0	19.0	−18	37	15	16	6	34	19

The parameters are: $V_{E_{UI}}$ ($V_{E_{DO}}$) and $V_{C_{UI}}$ ($V_{C_{DO}}$), earth-relative and cell-relative horizontal wind speed and direction of the updraught inflow (downdraught outflow); $Z_{E_{UI}}$ and $Z_{C_{UI}}$, earth-relative and cell-relative updraught inflow depth; $\Delta VR\lvert_{\Delta r=5\ km}$, radial difference of radial velocity over a 5 km distance; $SLOPE_{UI}$, slope of the updraught inflow; VR_{FUO} (VR_{RUO}), radial velocity of the updraught outflow exiting on the forward (rear) side of the cell; ΔX_{UO}, horizontal distance separating VR_{FUO} and VR_{RUO}; α_{UO}, elevation angle from the aircraft to the location of the updraught outflow; and Z_{TOP}, the echo top.

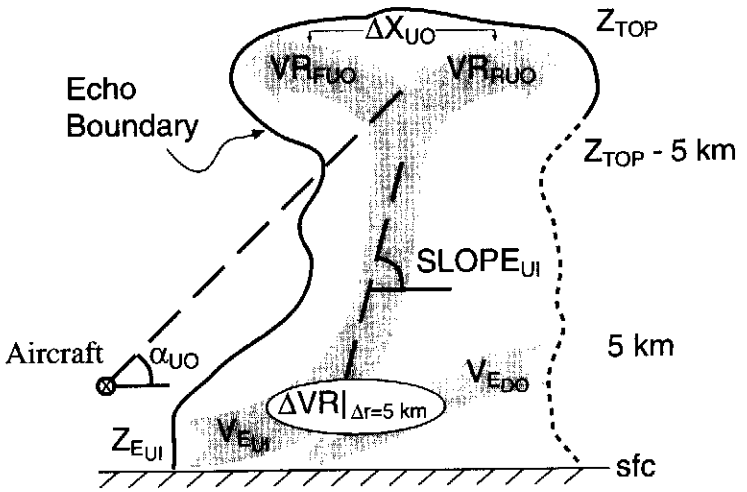

Figure 8. Conceptual model of airflow in convective updraughts and downdraughts. The parameters are: $Z_{E_{UI}}$, depth of the earth-relative updraught inflow; $\mathbf{V}_{E_{UI}}$, earth-relative horizontal wind speed and direction of the updraught inflow; $\mathbf{V}_{E_{DO}}$, earth-relative horizontal wind speed and direction of the downdraught outflow; $\Delta VR|_{\Delta r=5\ km}$, radial difference of radial velocity over a 5 km distance across the updraught–downdraught interface; $SLOPE_{UI}$, slope of the updraught inflow; VR_{FUO}, radial velocity of the updraught outflow exiting on the rear side of the cell; VR_{RUO}, radial velocity of the updraught outflow exiting on the rear side of the cell; ΔX_{UO}, horizontal distance separating VR_{FUO} and VR_{RUO}; α_{UO}, elevation angle from the aircraft to the location of updraught outflow; and Z_{TOP}, echo top. The short dashed portion of the echo boundary represents the fact that the convective cells are sometimes connected to larger regions of stratiform precipitation.

between distinct updraught–downdraught pairs. Therefore, updraught–downdraught pairs sometimes corresponded to the entire convective region of an MPF sampled by the aircraft. Alternatively, several MPFs contained updraught–downdraught pairs that extended over different subsets of the MPF domain, usually with different directional characteristics (viz. 921106A, 921214B, 921215A, 930118B and 930220A).

Although the conceptual model in Fig. 8 represents the airflow in a gust-front-relative sense, gust-front propagation characteristics generally could not be determined from the aircraft observations. Instead, we could only approximate the gust-front-relative motions by subtracting the previously discussed cell propagation vectors from the flow parameter vectors measured in an earth-relative sense. The earth-relative flow parameters are also important since they are the most relevant for fluxes at the ocean surface and to the large-scale momentum budget. Therefore, we include both earth-relative and cell-relative versions of the updraught inflow and downdraught outflow parameters in Table 4.

The horizontal wind parameters for the earth-relative updraught inflow and downdraught outflow ($\mathbf{V}_{E_{UI}}$, $\mathbf{V}_{E_{DO}}$) were tabulated from two sources. First, the maximum wind speeds were obtained from tail radar cross-sections (quasi range–height indicators) of the uninterpolated and unsmoothed single-Doppler radial velocity field. Wind directions were determined by examining the FAST dual-Doppler derived wind fields at altitudes near where the maximum wind speeds were observed. The maximum wind speeds associated with the earth-relative updraught inflow and downdraught outflow were not always observed in the same tail radar cross-section. For example, on a particular flight leg, the maximum values of earth-relative downdraught inflow might be best characterized by the fore scans of the tail radar, whereas the maximum values of earth-relative downdraught outflow might be best characterized by the aft scans of the tail radar. In this event, the different tail radar cross-sections used to characterize the earth-relative updraught inflow

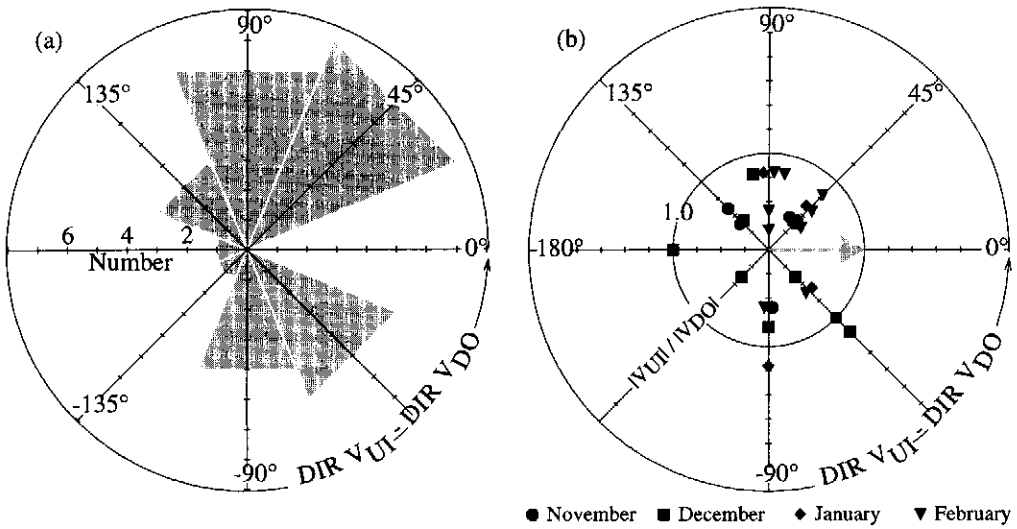

Figure 9. Comparison of the updraught inflow ($\mathbf{V}_{UI}$) with the downdraught outflow ($\mathbf{V}_{DO}$) in an earth-relative sense. (a) Polar histograms of the directional difference between earth-relative updraught inflow direction and earth-relative downdraught outflow direction. (b) Polar scatterplot of the ratio between earth-relative updraught inflow speed and earth-relative downdraught outflow speed as a function of directional difference. Data points are subdivided by month as indicated in the figure; the grey arrow represents a reference vector of unit length.

and downdraught outflow would be separated by 1 to 4 min, but would be representative of approximately the same spatial domain. The tail radar usually viewed the convective cells in a direction nearly normal to the updraught–downdraught interface, because the aircraft sampling strategy was to fly parallel to line segments of convection to best sample the flow normal to the line segment. As a result, a fore or aft scan would almost always lie within 20°–30° of the true flow plane of an earth-relative updraught inflow or downdraught outflow, which equates to a potential magnitude underestimate of 7–13%.

Examination of the high-resolution, uninterpolated single-Doppler tail radar cross-sections led to accurate determination of the depth of the earth-relative updraught inflow ($Z_{E_{UI}}$), the maximum radial difference of radial velocity across the updraught–downdraught interface ($\Delta V R|_{\Delta r=5\text{ km}}$), the maximum slope of the updraught inflow ($SLOPE_{UI}$), and the maximum echo top (Z_{TOP}). The tail cross-sections were also better for documenting the parameters associated with the updraught outflow (VR_{FUO}, VR_{RUO}, ΔX_{UO}, α_{UO}) because the observations were often at relatively large elevation angles rendering the dual-Doppler wind field analyses unreliable.

The maximum values of earth-relative horizontal wind speed in the 27 updraught inflows ($|\mathbf{V}_{E_{UI}}|$) ranged from 4 to 15 m s^{-1} with a dominant mode in the distribution between 5 and 10 m s^{-1} (Table 4). The maximum values of earth-relative horizontal wind speed in downdraught outflows ($|\mathbf{V}_{E_{DO}}|$) were larger, ranging from 7 to 20 m s^{-1} with a dominant mode in the distribution between 10 and 15 m s^{-1}. All but four of the updraught–downdraught pairs had $|\mathbf{V}_{E_{DO}}|$ greater than $|\mathbf{V}_{E_{UI}}|$ (Fig. 9(b)). This result is consistent with previous studies (Ulanski *et al.* 1973; Houze 1977; Johnson and Nicholls 1983; Young *et al.* 1995; Jorgensen *et al.* 1997) since it suggests that the convection increases the kinetic energy of the boundary layer, and that downdraught outflows systematically produce larger air–sea fluxes of sensible and latent heat than do updraught inflows, not only because of their depressed temperature and water-vapour content but also because of stronger surface wind speed.

The earth-relative wind directions associated with updraught inflow and downdraught outflows ($\mathbf{V}_{E_{UI}}$ and $\mathbf{V}_{E_{DO}}$) spanned 0–360° but more often than not contained some westerly component. The absolute value of the directional difference between $\mathbf{V}_{E_{UI}}$ and $\mathbf{V}_{E_{DO}}$ was most frequently 45° to 90° and rarely 0° or 180° (Fig. 9(a)).

The direction of $\mathbf{V}_{E_{UI}}$ is most similar to the large-scale wind direction between 1000 and 850 mb (Fig. 10(a) to (d)), further evidence that the updraught inflow is not simply a boundary-layer phenomenon. The distributions of directional difference further suggest that the large-scale winds turned clockwise (cyclonically for most cases) as they entered the updraught inflows. In addition, the maximum values of $|\mathbf{V}_{E_{UI}}|$ were generally greater than the large-scale wind speed, as evidenced by the high frequency of magnitude ratios less than one in Fig. 10(e) to (h). These trends may be related to acceleration of the large-scale winds by horizontal pressure gradients associated with the convection.

Figure 11(a) to (d) shows that the direction of $\mathbf{V}_{E_{DO}}$ is best correlated with the large-scale wind direction in the 1000–700 mb layer. The directional differences in these distributions are centred near 0°, with the best correspondence to the large-scale flow at 850 mb. The relatively broad distribution, and hence lack of strong correspondence, at 500 mb suggests that convective downdraughts do not transport the horizontal momentum of air from mid-levels to the surface. Downdraught outflows at the ocean surface evidently consist of air brought down from the lower tropospheric environment. Although this result should be interpreted with caution because of the possible influence of pressure-gradient forces, it is consistent with the thermodynamic data discussed in Kingsmill and Houze (1999). However, the maximum values of $|\mathbf{V}_{E_{DO}}|$ were almost always greater than the large-scale wind speed at 1000, 850, 700 and 500 mb (Fig. 11(e) to (h)). This is another indication of the possibility that the downdraughts increased the kinetic energy of the boundary layer.

Although an earth-relative perspective is more relevant for sea-surface fluxes and for momentum transports in the context of large-scale motions, a cell-relative or gust-front-relative coordinate system is necessary for a proper examination of the convective-cell dynamics. As mentioned earlier, we have measured the cell motions from the aircraft data and we assume that cell-relative motions also approximate the gust-front-relative motions.

Before comparing the updraught inflow and downdraught outflow in a cell-relative sense, it is first instructive to compare cell propagation with updraught inflow and downdraught outflow in an earth-relative sense. The directional difference between $\mathbf{V}_{PROP}$ and $\mathbf{V}_{E_{UI}}$ is most frequently 0° while the magnitude ratio $|\mathbf{V}_{PROP}|/|\mathbf{V}_{E_{UI}}|$ is widely scattered on both sides of the circle representing a ratio of 1.0 (Fig. 12). The directional difference between $\mathbf{V}_{PROP}$ and $\mathbf{V}_{E_{DO}}$ has a broader distribution but is still most commonly 0° (Fig. 13(a)). The magnitude ratio $|\mathbf{V}_{PROP}|/|\mathbf{V}_{E_{DO}}|$ is characterized by less scatter, values that are almost all less than 1.0, and an average of 0.58 (Fig. 13(b)). Interestingly, Goff (1976) obtained an average value of 0.67 for the ratio of gust-front propagation speed to wind speed behind 20 gust fronts observed in Oklahoma. Assuming that our $|\mathbf{V}_{E_{DO}}|$ corresponds to Goff's post gust-front wind speed, these results suggest that the propagation of convective cells observed by aircraft in COARE were determined by the propagation of gust-front interfaces.

The directions of cell-relative updraught inflow and downdraught outflow ($\mathbf{V}_{C_{UI}}$ and $\mathbf{V}_{C_{DO}}$ in Fig. 14(a)) tend to be orthogonal, intersecting at either −90° or +135°. The ratio of $|\mathbf{V}_{C_{UI}}|/|\mathbf{V}_{C_{DO}}|$ differed considerably from the corresponding earth-relative ratios in that a much greater fraction of the 27 updraught–downdraught pairs are characterized by values greater than 1.0 (Fig. 14(b)). Therefore, the magnitudes of $\mathbf{V}_{UI}$ and $\mathbf{V}_{DO}$ are more comparable in a cell-relative rather than earth-relative sense.

We did not attempt to measure the origination height of earth-relative downdraught outflows, because they usually exhibited a continuously downward slope within the ob-

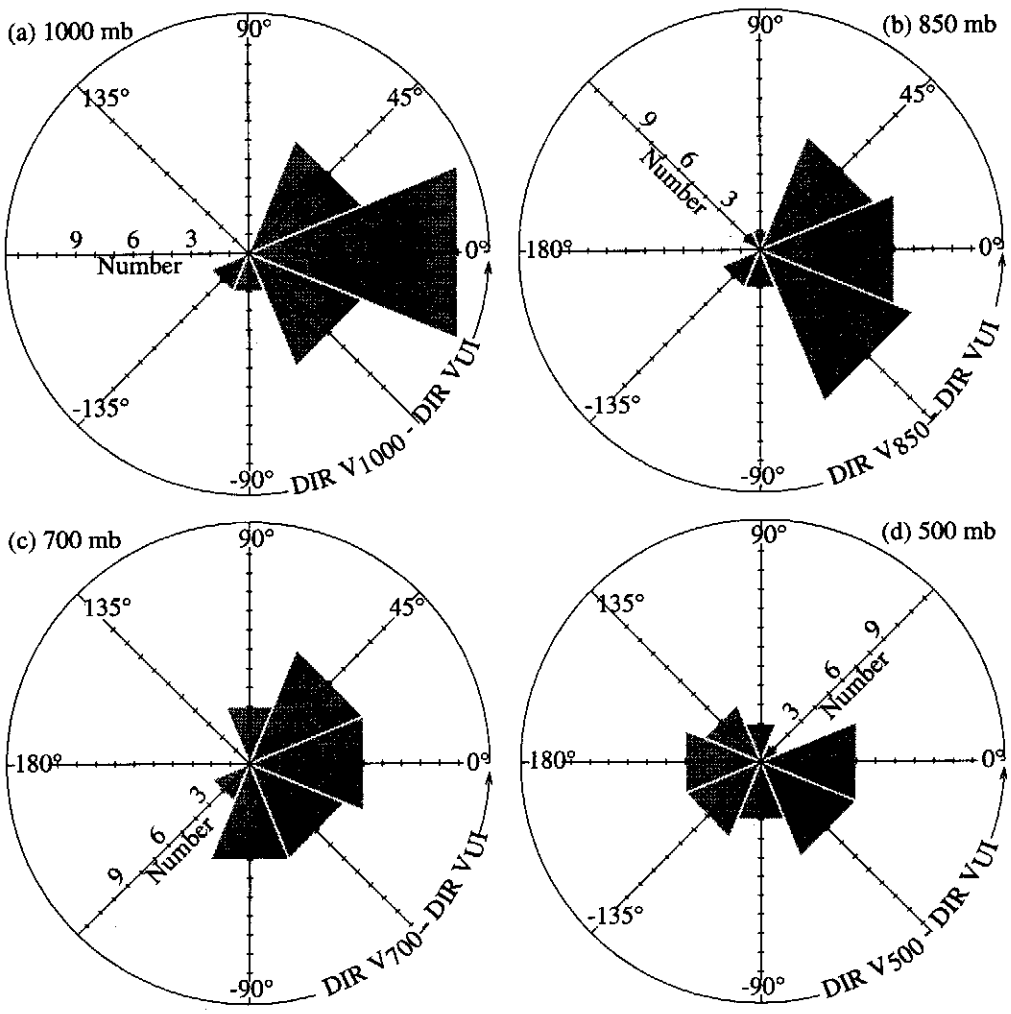

Figure 10. As Fig. 5 but a comparison of NCEP large-scale winds and updraught inflow (V_{UI}) in an earth-relative sense.

servational domain. The height of the earth-relative updraught inflow channel ($Z_{E_{UI}}$) was measured upstream of the updraught–downdraught interface and varied from 1 to 9 km on a case-to-case basis (Table 4). The echoes that were associated with the earth-relative updraught inflow prior to its upward deflection originated primarily from regions of stratiform precipitation, as the tail radars were insensitive to clear-air scatterers. Figure 6 shows an example of a deep updraught inflow (~9 km), with very strong inflow at the 5 km level, while the yellow channel of positive radial velocity on the right side of the radar in Fig. 15 is an example of a very shallow updraught inflow (~1 km).* These results together with the data in Table 4 suggest that all of the earth-relative updraught inflows were deeper than the tropical oceanic boundary layer. However, a knowledge of the cell-relative updraught inflow depth ($Z_{C_{UI}}$) is necessary for determining the vertical extent over which air is actually entering the convection.

* Note that the sign of low-level VR changes on the left side of the radar, which is consistent with the left-to-right motions implied by the updraught inflow on the right side of the radar.

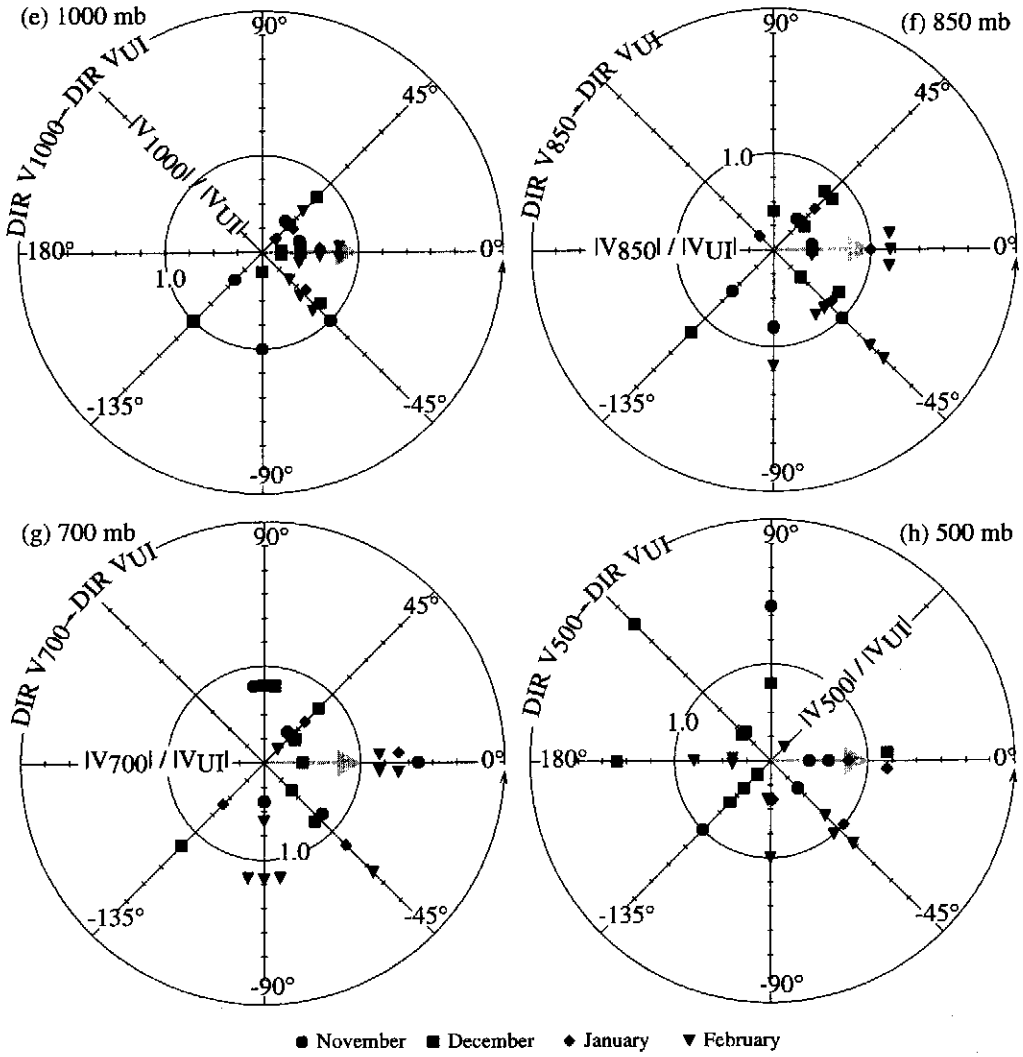

Figure 10. Continued.

Since $Z_{C_{UI}}$ was not directly measured during the tabulation of flow parameter characteristics, an indirect technique was devised to estimate this parameter. First, an earth-relative updraught inflow profile was developed for each case in Table 4 by incorporating information about the earth-relative updraught inflow depth ($Z_{E_{UI}}$), magnitude (MAX $|\mathbf{V}_{E_{UI}}|$), and direction (DIR $\mathbf{V}_{E_{UI}}$) as well as the magnitude of the forward updraught outflow (VR_{FUO}). A primary assumption in this technique is that the earth-relative updraught inflow profile is entirely in the same plane as DIR $\mathbf{V}_{E_{UI}}$. For the 930210BI case (Table 4), this means that the earth-relative updraught inflow profile is assumed to be entirely in the 315°–135° plane. The magnitude associated with the lowest levels of the profile is determined by MAX $|\mathbf{V}_{E_{UI}}|$. These values extend from the surface up to an altitude equal to $Z_{E_{UI}}/2$. Then, in the layer between $Z_{E_{UI}}/2$ and $3 \times Z_{E_{UI}}/2$, the magnitude of the earth-relative updraught inflow decreases linearly to a value equal to $-1 \times$ MAX $|\mathbf{V}_{E_{UI}}|$. Finally, in the layer between $3 \times Z_{E_{UI}}/2$ and Z_{TOP} (i.e. echo top), the inflow varies linearly

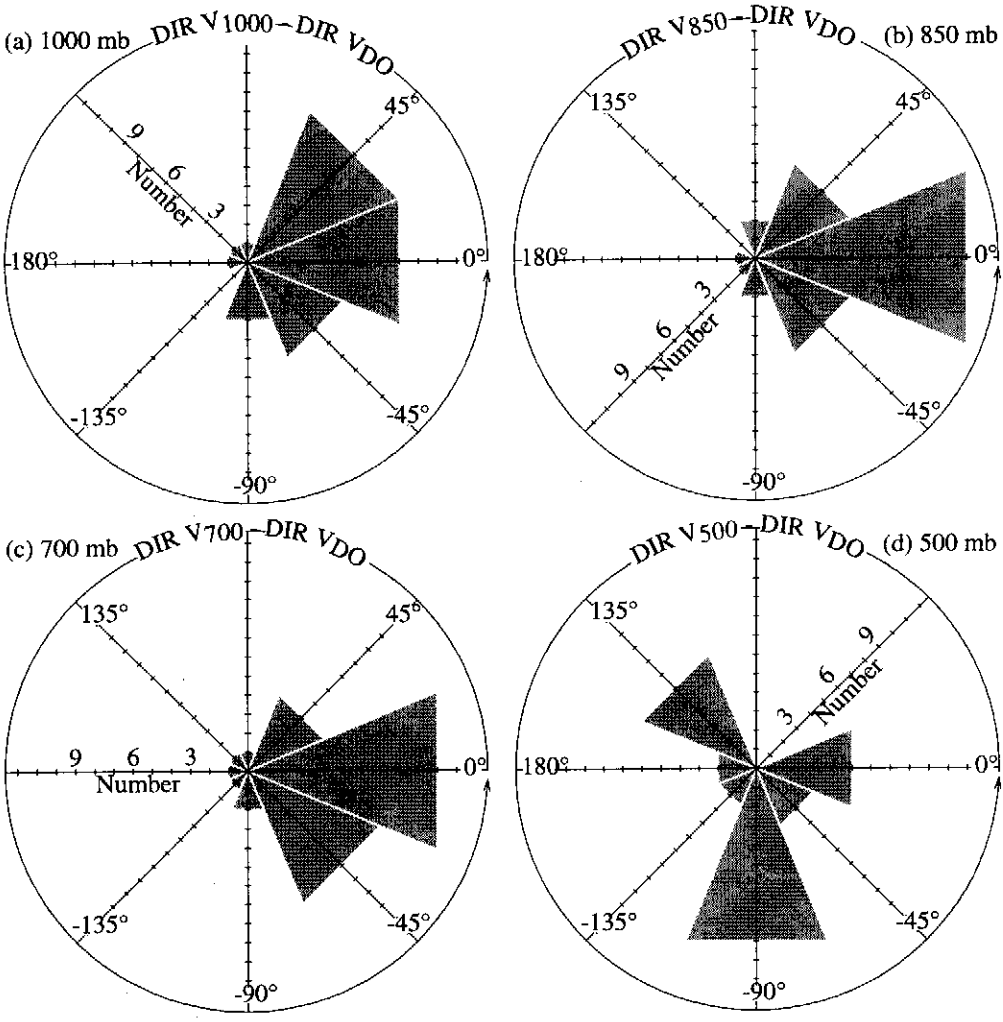

Figure 11. As Fig. 5 but a comparison of NCEP large-scale winds and updraught inflow ($\mathbf{V}_{DO}$) in an earth-relative sense.

between $-1 \times$ MAX $|\mathbf{V}_{E_{UI}}|$ and $-1 \times VR_{FUO}$. The earth-relative updraught inflow profile for the case on 930210BI is shown in Fig. 16(a). A cell-relative updraught inflow profile is obtained by subtracting the appropriate cell propagation vector (Table 3) from each level of the corresponding earth-relative updraught inflow profile, and then projecting the resulting vectors onto the plane defined by DIR $\mathbf{V}_{C_{UI}}$ (Table 4), the direction associated with the maximum cell-relative updraught inflow. For the 930210BI case, the profile is in the 341°–161° plane and is illustrated in Fig. 16(b). The altitude where the profile crosses from positive to negative values is an estimate of cell-relative updraught inflow depth ($Z_{C_{UI}}$). For 930210BI, this depth is about 9 km. Estimates of $Z_{C_{UI}}$ for the other cases are listed in Table 4.

The results of this exercise can be separated into two groups: cases where the earth-relative updraught inflow direction differed from the cell propagation direction, and cases where these directions were the same. In the former group (16 cases), $Z_{C_{UI}}$ was greater than $Z_{E_{UI}}$ by a factor of 1 to 19 (mean of 3.5), i.e. the cell-relative inflow was as deep or

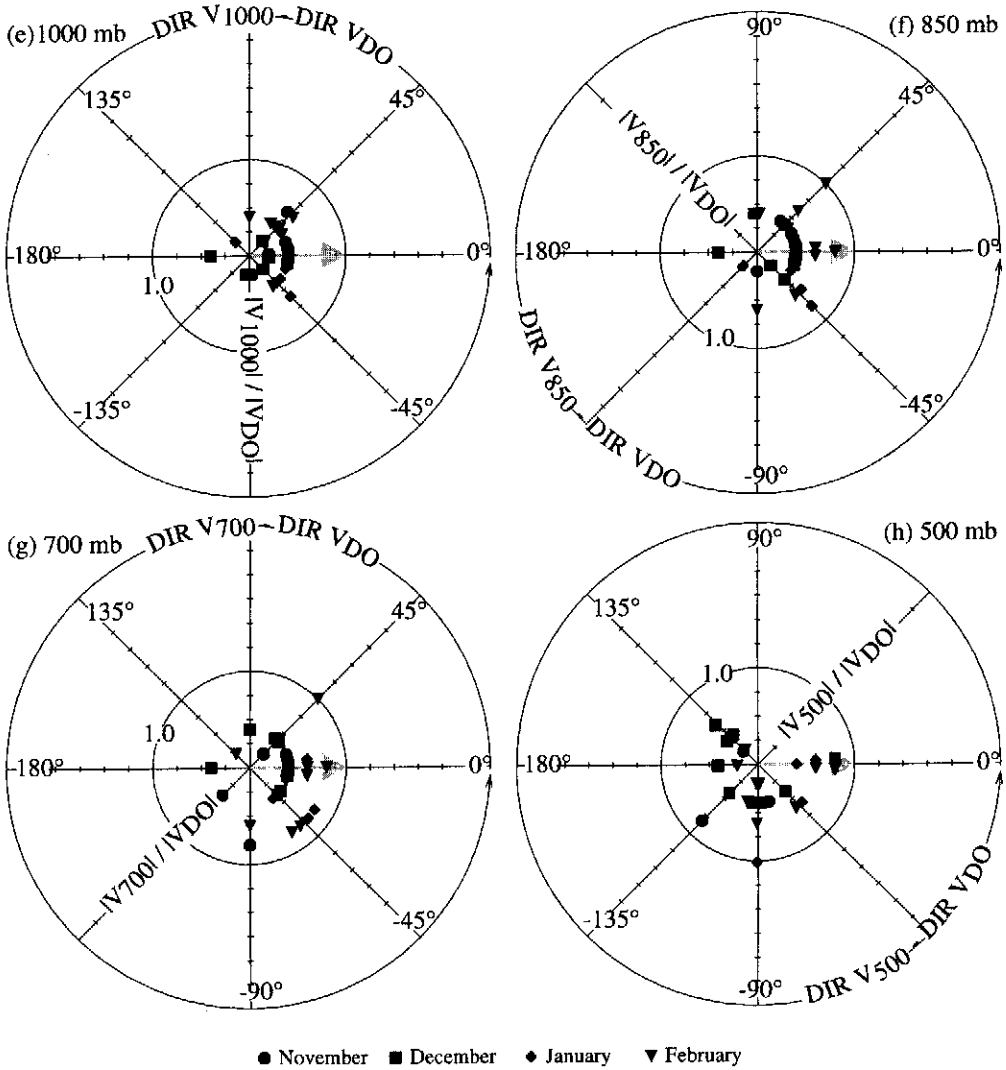

Figure 11. Continued.

deeper than the inflow layer in the earth-relative frame. In the latter group (11 cases), the interpretation is more complicated. When the earth-relative updraught inflow magnitude was greater than the cell propagation speed (8 cases), Z_{CUI} was less than Z_{EUI} by a factor of 0.5 to 0.8 (mean of 0.7). In these cases the cell-relative inflow layer is somewhat shallower than the earth-relative inflow layer, but not significantly. Thus, the estimated depths of the cell-relative inflow layer in 24 of 27 cases are of the same general value as the earth-relative depths. We therefore conclude that the deep updraughts sampled by the aircraft were generally drawn from a layer deeper than the tropical oceanic boundary layer.

When the earth-relative updraught inflow magnitude was less than the cell propagation speed (3 cases), our conceptual model of the updraught inflow was no longer valid, and the depth of the cell-relative inflow was indeterminable from the available information. This situation is more representative of the 'propagating' model of convection, where the

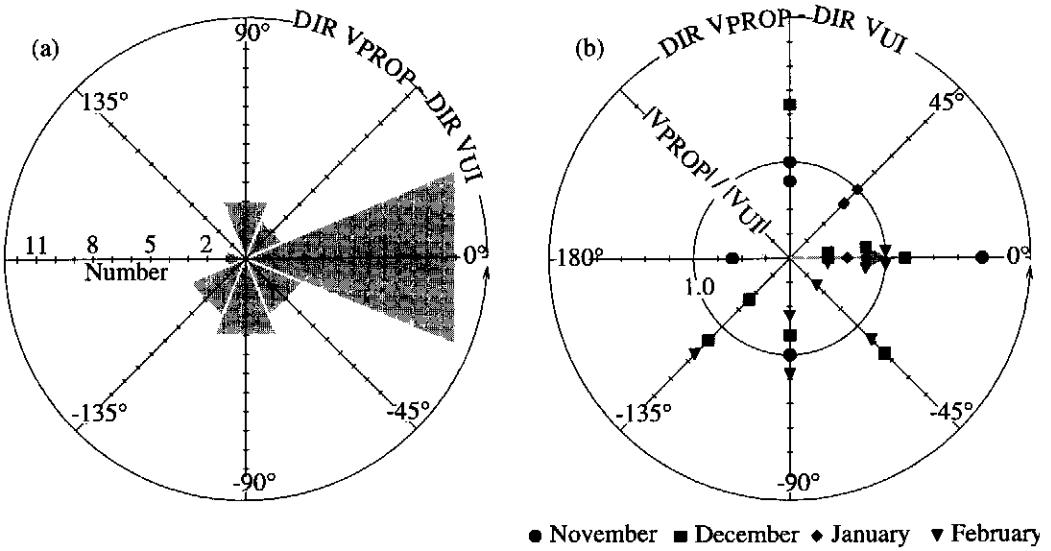

Figure 12. As Fig. 9 but a comparison of cell propagation (V_{PROP}) and updraught inflow (V_{UI}) in an earth-relative sense.

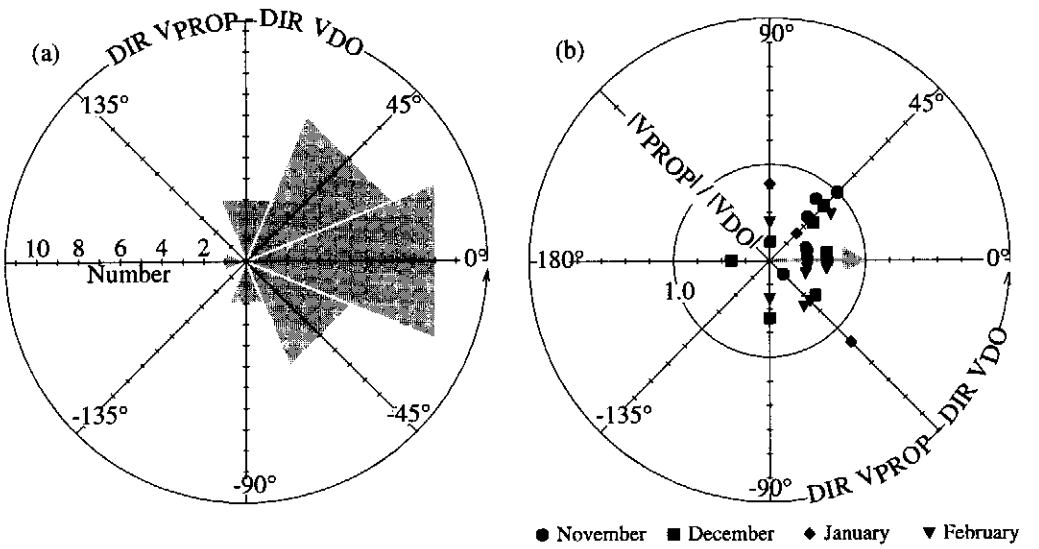

Figure 13. As Fig. 9 but a comparison of cell propagation (V_{PROP}) and downdraught outflow (V_{DO}) in an earth-relative sense.

convection travels relative to flow at all levels (Moncrieff 1981) rather than the 'jump' model with overturning circulations that we have been using. Therefore, these are cases where the assumptions of our cell-relative flow estimation may preclude a meaningful result (listed as NA in Table 4).

Although the assumptions used in the estimation of $Z_{C_{UI}}$ are necessarily crude, the results suggest that *a considerable amount of air from above the boundary layer enters the convection.* Zipser *et al.* (1981) and Jorgensen *et al.* (1991) have also observed deep inflows in tropical oceanic convection. The degree to which this ingested air ascends is

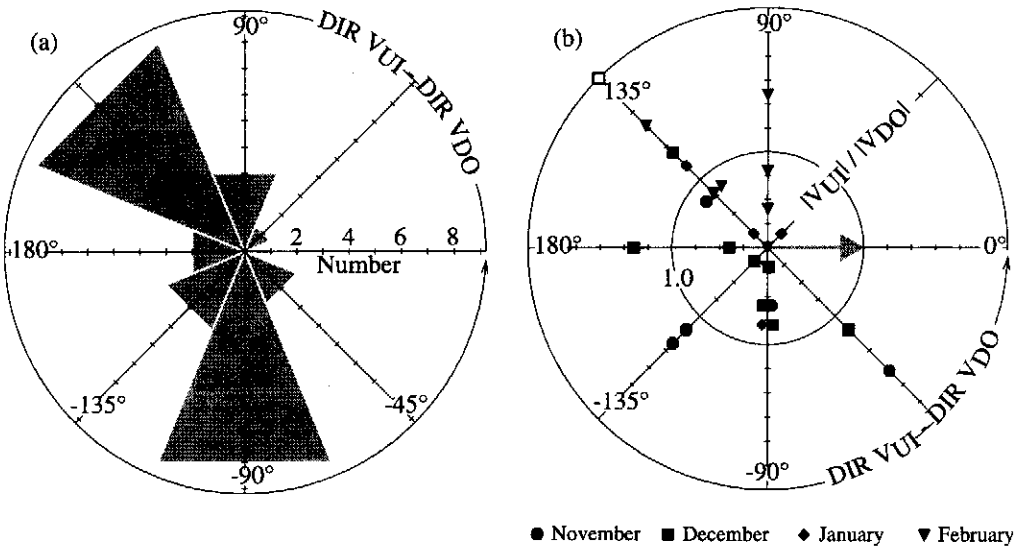

Figure 14. As Fig. 9 but a comparison of updraught inflow ($\mathbf{V}_{UI}$) and downdraught outflow ($\mathbf{V}_{DO}$) in a cell-relative sense.

dependent upon its thermodynamic characteristics, a subject that is addressed in Kingsmill and Houze (1999).

The maximum radial difference of radial velocity over a 5 km distance near the updraught–downdraught interface associated with the 27 updraught–downdraught pairs ($\Delta VR|_{\Delta r=5\text{ km}}$ in Table 4) varied from -11 to -22 m s^{-1}. There was a slight tendency for larger differences to be associated with deeper convection (MAX Z_{TOP} in Table 4). Relating values of $\Delta VR|_{\Delta r=5\text{ km}}$ to horizontal divergence must be done cautiously, since they represent the airflow only in the plane of the cross-section. However, the dual-Doppler wind fields indicate that the horizontal convergence at the low levels of these updraught–downdraught pairs was dominated by the component across the updraught–downdraught interface. Figure 17 shows the horizontal context of the updraught–downdraught pair documented in Figs. 6 and 7. The aircraft track was parallel to a line segment of convection, and the line AB shows the horizontal component of the beam of the tail radar. Figure 6 shows the reflectivity and radial velocity along AB and Fig. 7 shows the dual-Doppler derived divergence and vertical velocity fields along AB. Figure 17 shows the low-level and upper-level flow, respectively. At low levels, the updraught–downdraught interface was ~10 to 15 km west of, and oriented approximately parallel to, the aircraft flight track indicated by the blue line. The vector wind field indicates that the cross-front component of horizontal wind contributes much more to the convergence than the along-front component of horizontal wind. As discussed earlier, the tail radar usually viewed the convective cells in a direction nearly normal to the updraught–downdraught interface (e.g. line AB in Fig. 17). The values of $\Delta VR|_{\Delta r=5\text{ km}}$ should provide a good estimate of the horizontal divergence because they were obtained in this manner, and they have not been filtered by the interpolation process.

The slope of the updraughts in the convective cells often varied by more than 45° over distances as small as 10 km, with maximum values in the range of 30°–80° (Table 4), where 90° is defined as vertical. LeMone *et al.* (1984b) measured values of slope in the range of 20° to 35° for MPFs observed during GATE. However, their observations were based upon in situ aircraft data, and are probably more representative of overall MPF

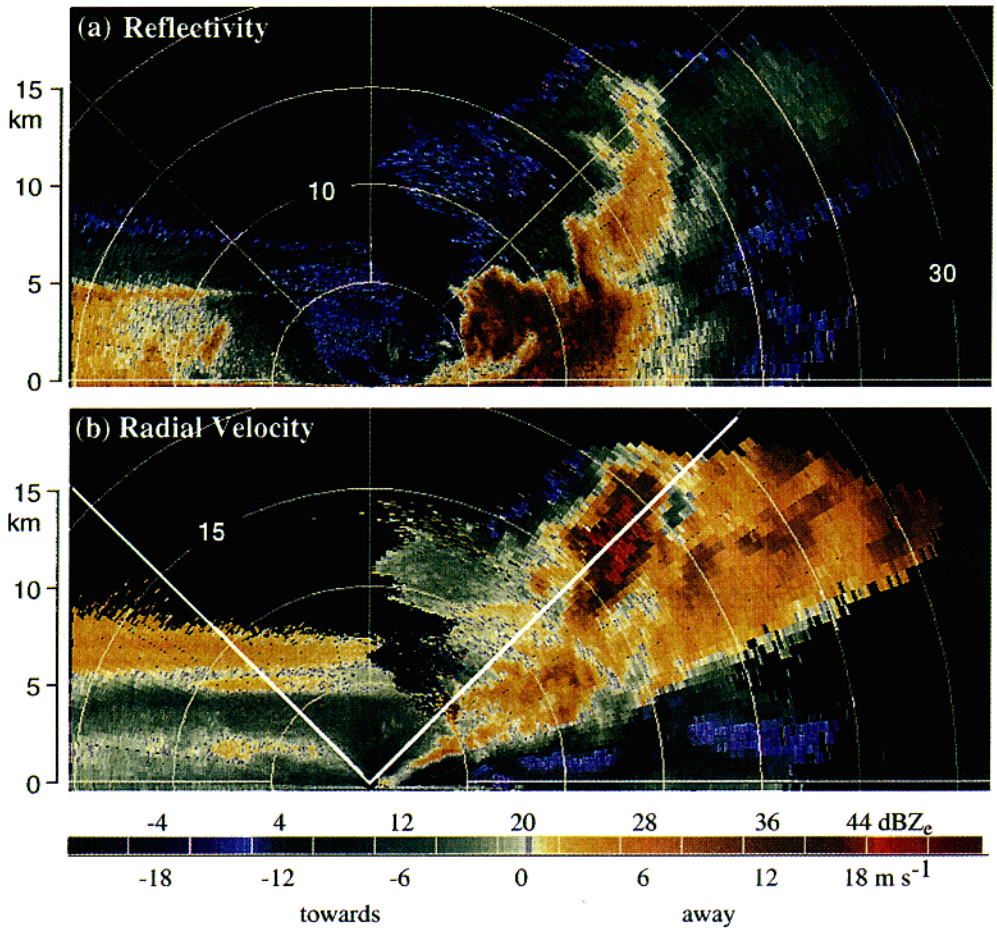

Figure 15. As Fig. 6 but for 9 February 1993 at 1744.50 UTC. Bold lines in (b) indicate 45° (see discussion of Fig. 6).

slope than the slope of individual convective cells or updraughts. In the data of this study, there was no correlation between maximum updraught slope and maximum echo top when analysing the convective cells collectively. However, the lack of correlation may be related to the effects of attenuation, which limits the accuracy of radar-detected echo top. Also, as suggested by the model results of Rotunno *et al.* (1988), the slope of updraughts probably varied as a function of the stage of evolution of a convective cell.

Updraught outflows were generally concentrated in the 5 km just below echo top, and were usually observed at large elevation angles with respect to the aircraft (α_{UO} in Table 4). Therefore, three-dimensional wind fields often could not be synthesized from the airborne Doppler radar measurements in the outflow regions. Those few updraught outflows captured in the dual-Doppler derived wind fields showed that both components of the horizontal wind contributed to the horizontal divergence (e.g. Fig. 17(b)), in stark contrast to the dominance of the horizontal convergence at the interface between updraught inflow and downdraught outflow by the cross-gust-front component of horizontal wind at low levels (e.g. Fig. 17(a)). In any one tail radar cross-section, the updraught outflow typically produced a pattern with two radial velocity maxima in which V_R $_{FUO}$ was on the

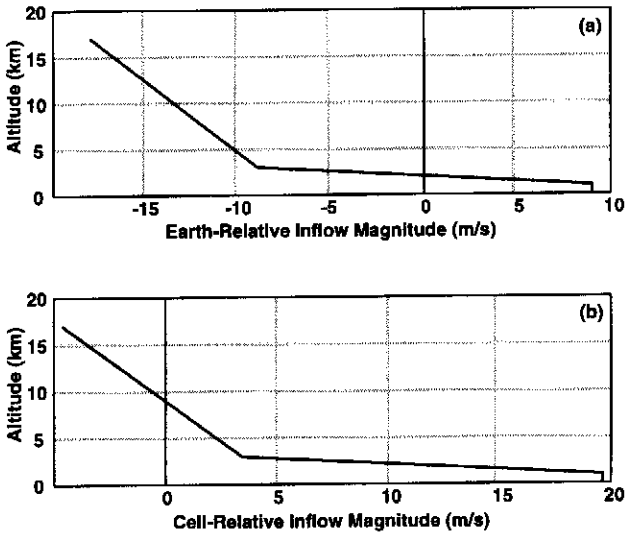

Figure 16. Estimated vertical profiles of (a) earth-relative and (b) cell-relative updraught inflow magnitude for the 930210B1 case (see Table 4). The earth-relative profile was calculated in the 315°–135° plane, and the cell-relative profile in the 341°–161° plane, and the cell-relative profile in the 341°–161° plane.

same side of the cell as the updraught inflow with values opposite in sign to VR_{UI}, while VR_{RUO} was on the same side of the cell as the downdraught outflow with values opposite in sign to VR_{DO} (Fig. 8). The absolute values of VR_{FUO} and VR_{RUO} were broadly distributed, ranging from 2 to 26 m s^{-1}, and were separated (ΔX_{UO}) by a distance that varied from 3 to 13 km (Table 4). There was a tendency for the most intense updraught outflows, those with the largest sum of $|VR_{FUO}|$ and $|VR_{RUO}|$, to be associated with the greatest separation distances (Fig. 18(a)). The most intense updraught outflows also tended to be associated with the deepest convective cells (Fig. 18(b)). This relationship remains evident when the updraught outflow intensity is normalized by the separation distance (Fig. 18(c)).

5. Air motions in stratiform precipitation regions

In stratiform precipitation, the radial velocity data also indicated the presence of inflows and outflows. However, they extended over larger horizontal distances than in convective cells. The most distinctive and recurring of these structures were inflows originating in mid-levels. They were evident as thin, gradually descending channels of VR and would usually begin at the base of an anvil. In this paper, the term anvil refers to radar echo aloft, i.e. precipitation aloft but not reaching the sea surface (virga). Usually, an echo aloft extended laterally from a region of deeper stratiform precipitation echo, where echo extended down to the sea surface.

Figure 19 shows an example of a stratiform radar echo with a bright band extending across an 80 km wide region. The bright band is most well defined near the aircraft, where the radar resolution is greatest. An anvil is evident on the right side of Fig. 19(a). The downward sloping, blue channel of negative VR at the base of the anvil (Fig. 19(b)) is a stratiform-region inflow channel. It extended into the interior of the precipitation region. As the stratiform inflow passed below the bright band at about the location of the aircraft it became evident as a thin, yellow channel of positive VR on the left side of Fig. 19(b). Adjacent to the mid-level inflow were two less well-defined stratiform outflows: one

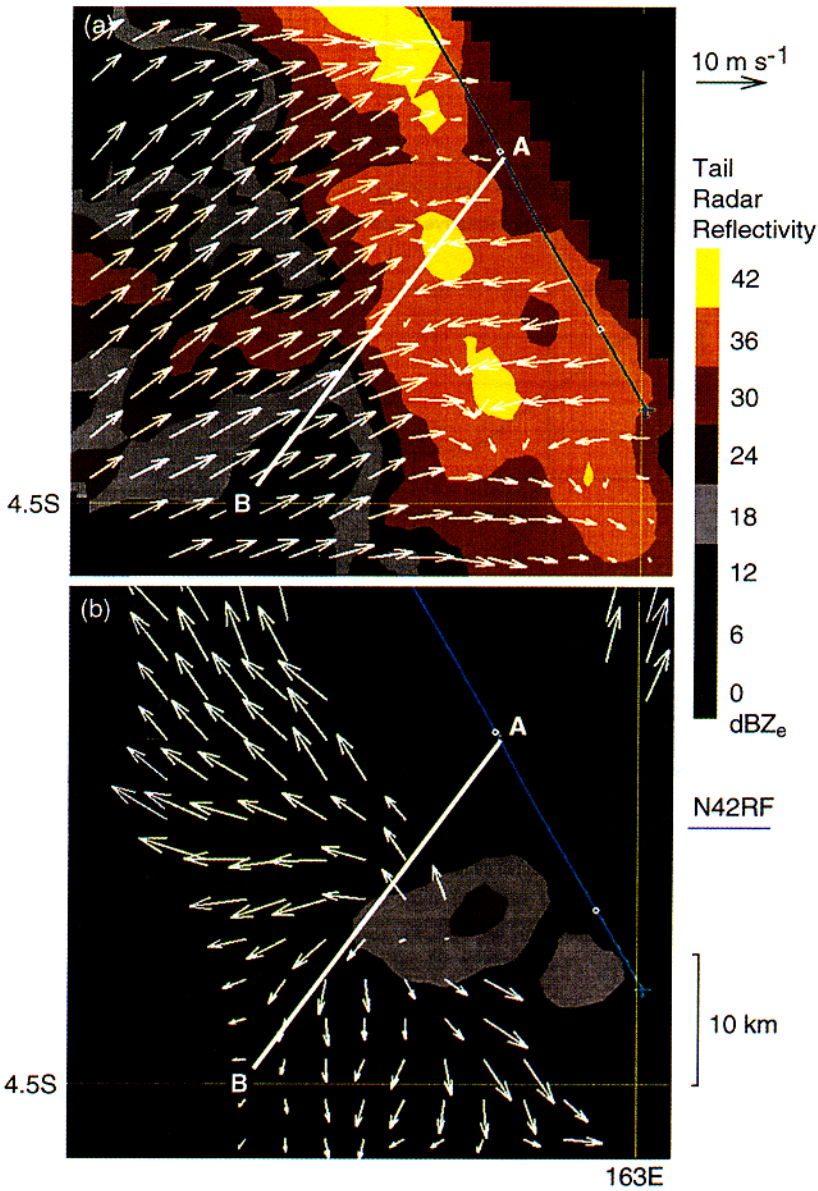

Figure 17. Dual-Doppler derived horizontal cross-sections of earth-relative horizontal winds overlaid on tail radar reflectivity at altitudes of (a) 3.6 km and (b) 14.8 km on 14 December 1992 at 1630 UTC. The line segment AB refers to the tail radar vertical cross-section in Fig. 6 and the dual-Doppler derived vertical cross-section in Fig. 7. The colour key indicates values of reflectivity in dBZ_e.

immediately above the stratiform inflow and another near the surface. These are evident in Fig. 19(b) as thicker channels of positive and negative VR on the right and left of the figure, respectively. Both of these features form strong vertical gradients of VR where they bound the stratiform inflow. In most cases, the shear interface with the upper stratiform outflow was the sharper of the two.

We examined all of the tail Doppler radar data from the 25 aircraft missions to locate stratiform circulation features similar to those just described. To aid in recognizing these

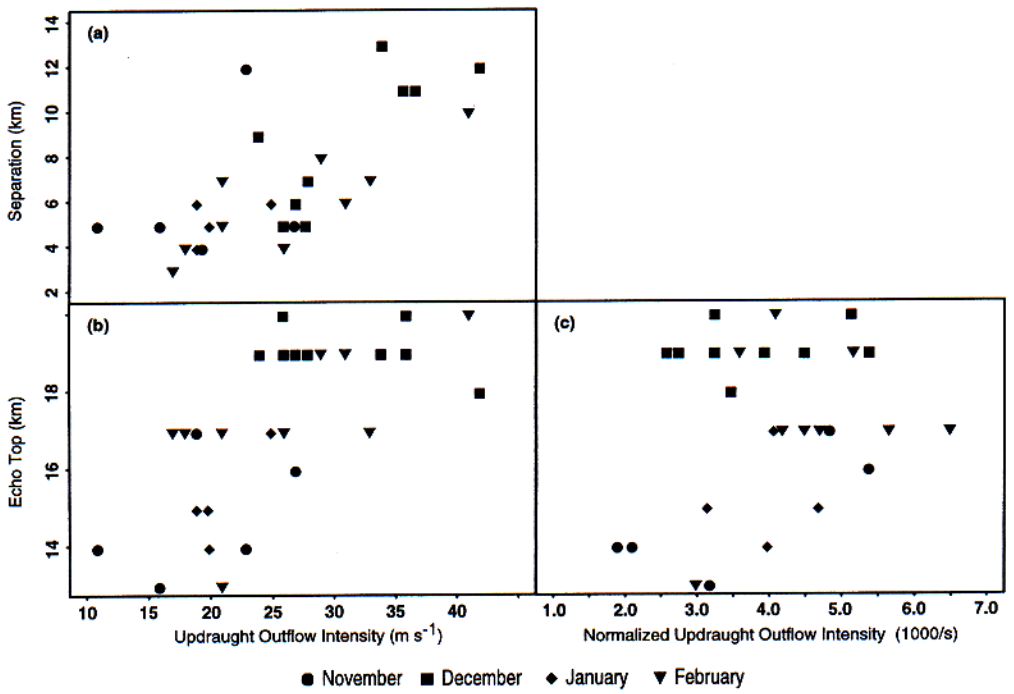

Figure 18. Scatterplots of (a) maximum earth-relative updraught outflow intensity ($|\mathbf{VR}_{FUO}| + |\mathbf{VR}_{RUO}|$) versus updraught outflow separation distance (ΔX_{UO}), (b) maximum earth-relative updraught outflow intensity versus maximum echo top (Z_{TOP}) and (c) normalized maximum earth-relative updraught outflow intensity ($[|\mathbf{VR}_{FUO}| + |\mathbf{VR}_{RUO}|]/\Delta X_{UO}$) versus maximum echo top.

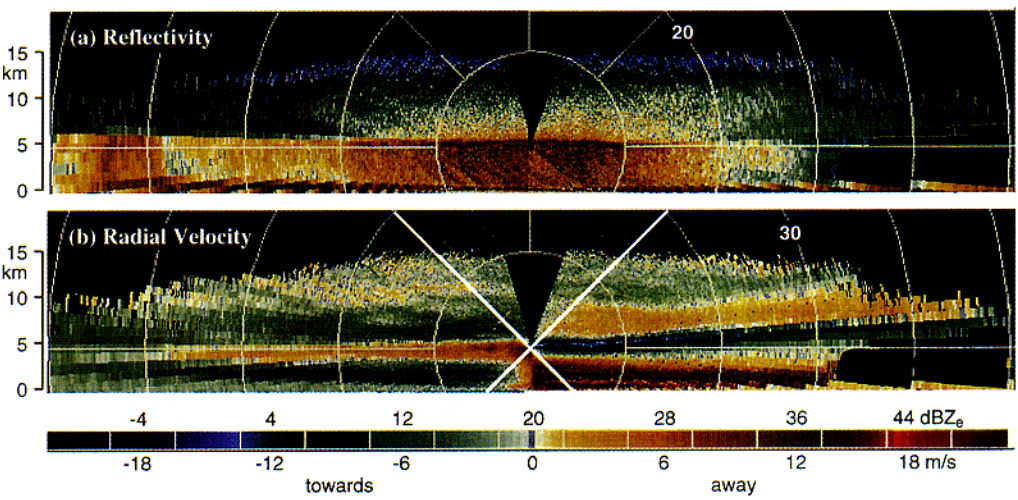

Figure 19. As Fig. 6 but for 14 December 1992 at 1831.33 UTC. Range rings are at 10 km intervals. Bold lines in (b) indicate 45° angles (see discussion of Fig. 6).

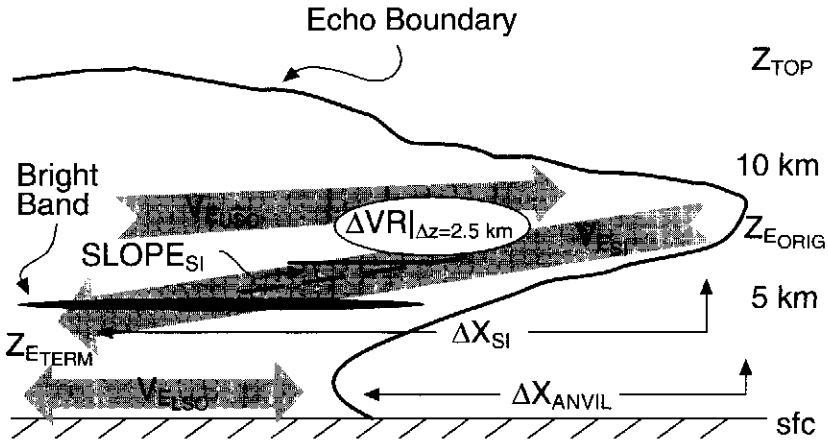

Figure 20. Conceptual model of airflow in stratiform precipitation regions. The parameters are: $\mathbf{V}_{E_{SI}}$, earth-relative horizontal wind speed and direction of the stratiform inflow; $\mathbf{V}_{E_{USO}}$, earth-relative horizontal wind speed and direction of the upper stratiform outflow; $\mathbf{V}_{E_{LSO}}$, earth-relative horizontal wind speed and direction of the lower stratiform outflow; $\Delta VR|_{\Delta z=2.5\ km}$, vertical shear of radial velocity over a 2.5 km distance above or below the stratiform inflow; $Z_{E_{ORIG}}$, earth-relative origination height of the stratiform inflow; $Z_{E_{TERM}}$, earth-relative termination height of the stratiform inflow; ΔX_{SI}, horizontal extent of the stratiform inflow; $SLOPE_{SI}$, slope of the stratiform inflow; ΔX_{ANVIL}, horizontal extent of anvil; and Z_{TOP}, echo top.

patterns we formulated a simplified model of the inflow and outflow structures in stratiform precipitation (Fig. 20). Tail cross-sections, such as Fig. 19, and FAST dual-Doppler wind field analyses were examined to determine the values of those parameters (defined in the appendix) for 22 different stratiform precipitation inflow/outflow structures observed by the tail Doppler radars (Table 5). Most MPFs contained only one of these structures. However, multiple stratiform precipitation inflow/outflow structures did exist in three MPFs (viz. 921213A, 921214A and 930220A). They were distinguishable by the spatial continuity of their reflectivity and velocity patterns.

Unlike the stratiform inflow and upper stratiform outflow, the lower stratiform outflow is represented by arrowheads at both ends in Fig. 20. As will become apparent, this is meant to indicate the lack of correlation that the direction of this flow feature exhibits with respect to any of the other flow parameters.

Figure 20 models the stratiform-region airflow relative to the moving convective system. System motions of MPFs sample by the aircraft are difficult to quantify because of their usually complex structures and discrete modes of propagation. To be consistent with the convective cell analysis, we used a cell-relative framework to approximate the system-relative motions. Both earth-relative and cell-relative versions of the stratiform inflow and outflow parameters are listed in Table 5.

The tabulation of parameters for earth-relative stratiform inflows and outflow ($\mathbf{V}_{E_{SI}}$, $\mathbf{V}_{E_{USO}}$, $\mathbf{V}_{E_{LSO}}$) incorporated information from the dual-Doppler wind fields and the uninterpolated tail radar cross-sections. As with the convective cell airflow parameters, maximum wind speeds were determined from the uninterpolated tail radar cross-sections. Wind directions were then determined from examining the dual-Doppler wind fields at altitudes near to where the maximum wind speed occurred. For a given stratiform inflow/outflow structure, several tail cross-sections were examined to determine: the maximum vertical shear of radial velocity above or below the stratiform inflow ($\Delta VR|_{\Delta z=2.5\ km}$); the origination and termination heights of the earth-relative stratiform inflow ($Z_{E_{ORIG}}$, $Z_{E_{TERM}}$); the

TABLE 5. CHARACTERISTICS OF AIRFLOW PARAMETERS ASSOCIATED WITH STRATIFORM PRECIPITATION

CASE	$Z_{E_{ORIG}}$ (km)	$Z_{E_{TERM}}$ (km)	MAX ΔX_{SI} (km)	MAX $SLOPE_{SI}$ (deg)	MAX ΔX_{ANVIL} (km)	Earth-relative MAX $\lvert V_{E_{SI}}\rvert$ (m s^{-1})	Earth-relative DIR $V_{E_{SI}}$ (deg)	Cell-relative MAX $\lvert V_{C_{SI}}\rvert$ (m s^{-1})	Cell-relative DIR $V_{C_{SI}}$ (deg)	Earth-relative MAX $\lvert V_{E_{USO}}\rvert$ (m s^{-1})	Earth-relative DIR $V_{E_{USO}}$ (deg)	Cell-relative MAX $\lvert V_{C_{USO}}\rvert$ (m s^{-1})	Cell-relative DIR $V_{C_{USO}}$ (deg)	Earth-relative MAX $\lvert V_{E_{LSO}}\rvert$ (m s^{-1})	Earth-relative DIR $V_{E_{LSO}}$ (deg)	Cell-relative MAX $\lvert V_{C_{LSO}}\rvert$ (m s^{-1})	Cell-relative DIR $V_{C_{LSO}}$ (deg)	MAX $\Delta VR\lvert_{\Delta z=2.5\text{ km}}$ (m s^{-1})	MAX Z_{TOP} (km)
921102A I*	8	4	50	−6	75	13	270	10	253	8	45	9	73	5	315	1	315	17	13
921106A I*	8	4	55	−5	25	12	180	14	147	7	90	15	90	5	225	5	130	12	14
921119A I*	7	6	>70	−1	60	12	225	14	252	7	180	9	239	7	135	1	135	13	11
921126A I	8	5	>75	−3	50	17	135	NA	NA	9	90	NA	NA	3	315	NA	NA	14	10
921212A I*	8	0	165	−3	>55	26	90	24	84	8	135	5	135	7	0	10	346	13	15
921213A I*	7	5	40	−3	0	7	180	17	180	13	315	9	266	8	315	7	234	14	14
921213A II*	7	3	>75	−3	35	16	90	19	121	7	0	3	180	8	315	7	234	20	14
921214A I	7	5	>45	−3	>5	11	45	18	45	5	90	11	64	9	225	2	225	15	16
921214A II	8	5	40	−4	0	12	135	14	105	5	90	11	64	9	225	2	225	11	16
921214B I*	8	5	>70	−3	>25	14	90	20	90	6	225	5	158	17	315	13	333	20	15
921214C I*	8	5	50	−3	15	8	315	7	38	5	225	7	118	9	270	1	90	8	15
921216A I	8	5	25	−8	20	12	45	19	45	9	180	6	133	8	225	1	225	19	15
930117A I	5	4	35	−2	30	12	45	8	45	10	135	11	159	6	45	2	45	16	12
930118A I	6	4	30	−4	25	5	45	7	31	7	180	5	180	12	135	10	126	14	12
930118B I*	6	0	20	−11	10	13	135	8	135	8	0	12	344	9	135	4	135	15	15
930206C I	6	0	85	−5	45	17	315	8	315	12	0	9	52	6	0	7	96	8	15
930209A I*	7	5	>80	−1	>65	10	135	12	104	5	90	10	66	13	270	10	295	11	16
930209B I*	7	4	80	−3	35	13	135	15	106	6	45	13	45	20	225	13	225	15	16
930210A I*	4	1	>80	−2	50	16	225	9	225	12	135	14	106	5	270	5	356	20	12
930210B I*	4	0	60	−4	10	21	225	15	260	13	315	23	337	13	225	10	288	26	15
930220A I*	9	4	>45	−6	15	16	315	11	352	5	225	7	119	12	270	2	270	19	16
930220A II*	8	5	60	−3	50	10	315	8	21	8	225	7	144	9	315	7	28	19	15

The parameters are: $Z_{E_{ORIG}}$ ($Z_{E_{TERM}}$), earth-relative origination (termination) height of the stratiform inflow; ΔX_{SI}, horizontal extent of the stratiform inflow; $SLOPE_{SI}$, slope of the stratiform inflow; ΔX_{ANVIL}, horizontal extent of anvil; $V_{E_{SI}}$ ($V_{C_{SI}}$), earth-relative (cell-relative) horizontal wind speed and direction of the upper stratospheric outflow; $V_{E_{LSO}}$ ($V_{C_{LSO}}$), earth-relative (cell-relative) horizontal wind speed and direction of the lower stratiform outflow; $\Delta VR\lvert_{\Delta z=2.5\text{ km}}$, vertical shear of radial velocity over a 2.5 km distance; and Z_{TOP}, the echo top.

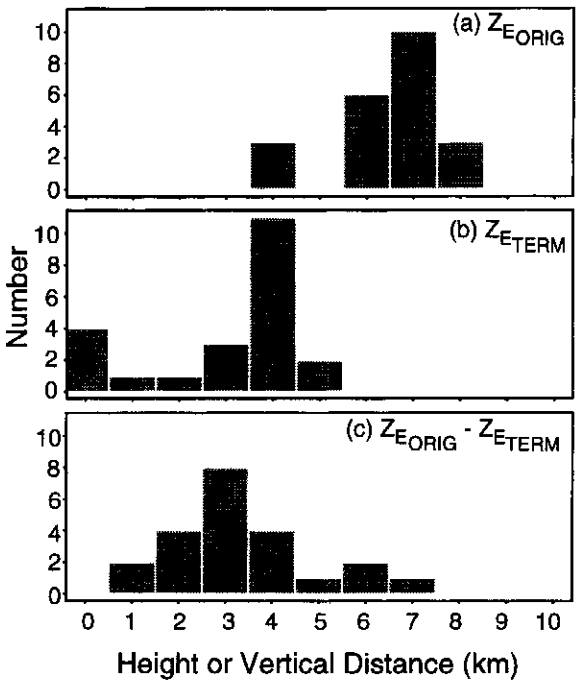

Figure 21. Histograms of earth-relative (a) origination height ($Z_{E_{ORIG}}$), (b) termination height ($Z_{E_{TERM}}$) and (c) vertical extent ($Z_{E_{ORIG}} - Z_{E_{TERM}}$) for stratiform inflows.

maximum horizontal extent of the stratiform inflow (ΔX_{SI}); the maximum slope of the stratiform inflow ($SLOPE_{SI}$); the maximum horizontal extent of anvil (ΔX_{ANVIL}); and the maximum echo top (Z_{TOP}).

Figure 21 indicates that stratiform inflows most frequently originated at about the 7–8 km level. The distribution of termination heights was broader, with a primary mode at the 4–5 km level and a secondary mode near the surface. Figure 19 is an example of a stratiform inflow that descends no further than an altitude of 4.5 km. Most stratiform inflows descended about 3 km.

The maximum horizontal extent of stratiform inflows (ΔX_{SI}) varied from 20 to 165 km, but most were in the range of 40 to 80 km (Table 5). However, many of the values represent only portions of stratiform inflows, which extended outside of the tail Doppler radar observing domain (hence, table entries are denoted >). Similarly, the maximum horizontal extent of anvil reflectivity features (ΔX_{ANVIL}) ranged from 0 to 75 km, but these values are lower limits. Subject to the limitations in interpreting these parameters, the results indicate that the maximum ΔX_{SI} exceeded the maximum ΔX_{ANVIL} in all but one case. This suggests that almost all of the stratiform inflows began on the underside of an anvil, and extended at least part way into a precipitating region. Combining the horizontal and vertical extent measurements yield maximum values of $SLOPE_{SI}$ that ranged from $-1°$ to $-11°$, but were most commonly around $-3°$ (Table 5).

The maximum values of earth-relative wind speed in the 22 stratiform inflows ($|\mathbf{V}_{E_{SI}}|$) varied from 5 to 26 m s^{-1} with most values from 10 to 15 m s^{-1} (Table 5). Cell-relative stratiform inflow magnitudes ($|\mathbf{V}_{C_{SI}}|$) were characterized by a distribution that was somewhat narrower overall (7–24 m s^{-1}) but one that did not have a distinct mode. These Doppler-radar-observed cell-relative stratiform inflow magnitudes are comparable

to system-relative rear inflow magnitudes observed by Doppler radar over continents in both midlatitudes (Smull and Houze 1987; Klimowski 1994) and the tropics (Chong *et al.* 1987; Keenan and Carbone 1992), but generally greater than those suggested by limited sounding data in the vicinity of tropical oceanic squall lines (Zipser 1969; Gamache and Houze 1982; Barnes and Sieckman 1984; Alexander and Young 1992). It appears that the finer-scale sampling in time and space by the Doppler radar may be required to determine the intensity of the mid-level stratiform region inflow.

The maximum values of $|\mathbf{V}_{E_{SI}}|$ were generally higher than earth-relative stratiform outflow magnitudes ($|\mathbf{V}_{E_{USO}}|$, $|\mathbf{V}_{E_{LSO}}|$), especially with respect to the upper stratiform outflows. The maximum values of vertical shear across the interfaces between these inflows and outflows ($\Delta VR|_{\Delta z=2.5\text{ km}}$) varied between 8 and 26 m s^{-1} over a 2.5 km vertical distance (Table 5). There were no distinct peaks in this distribution and no clear correlation with $|\mathbf{V}_{SI}|$.

The stratiform inflows and outflows came from nearly all directions, without any clear preferences (Table 5). The direction of $\mathbf{V}_{E_{SI}}$ is best related to the large-scale winds at 400–500 mb (Fig. 22(a) to (d)). These levels correspond well with the 4–7 km layer where most stratiform inflows were observed (Fig. 21). This result further indicates that the large-scale environmental wind determines the direction of the mid-level inflow. The distribution of directional differences at 400–500 mb are negatively skewed, suggesting that the large-scale winds at these levels turned clockwise (in most cases cyclonically) as they entered the stratiform inflows. In addition, the maximum values of $|\mathbf{V}_{E_{SI}}|$ were generally greater than the large-scale wind speed as is evident from the high frequency of magnitude ratios less than 1 in Fig. 22(e) to (h). These results suggest that horizontal pressure gradients within the stratiform precipitation were accelerating the large-scale winds as they penetrated the system.

The relationship between different flow parameters within stratiform precipitation is complicated. For example, the distribution of directional differences between $\mathbf{V}_{C_{SI}}$ and $\mathbf{V}_{C_{LSO}}$ as well as $\mathbf{V}_{C_{LSO}}$ and $\mathbf{V}_{C_{USO}}$ shows no dominant peaks. However, the distribution of directional difference between $\mathbf{V}_{C_{SI}}$ and $\mathbf{V}_{C_{USO}}$ peaks at absolute values of 45 to 135° (Fig. 23(a)). Similar to the relationship between $\mathbf{V}_{C_{UI}}$ and $\mathbf{V}_{C_{DO}}$ (Fig. 14(a)), these results suggest that stratiform precipitation regions are characterized by some degree of orthogonality of inflow and outflow. This similarity to characteristics of the airflow in convective cells is also evident by virtue of the fact that the magnitudes of $\mathbf{V}_{USO}$ and $\mathbf{V}_{SI}$ are more comparable in a cell-relative rather than earth-relative sense (Fig. 23(b)). Together, these points raise the question of how airflow parameters in the stratiform precipitation region of an MPF are related to the airflow parameters associated with the convective cells of the same MPF.

6. Relationship between the air motions in convective cells and stratiform precipitation regions

As discussed and documented above, the kinematic structures associated with convective cells and stratiform precipitation were distinctly different. However, these regions were often connected to one another. The dashed line on the right side of Fig. 8 and the open end on the left side of Fig. 20 are implicit indicators of this fact. Many of the convective cells documented in Table 4 occurred within the same MPF as the stratiform precipitation regions documented in Table 5. These cases are indicated by the asterisks in each table. By comparing the airflow parameters associated with convective cells against those associated with stratiform precipitation, we can infer how these kinematic structures may relate to one another.

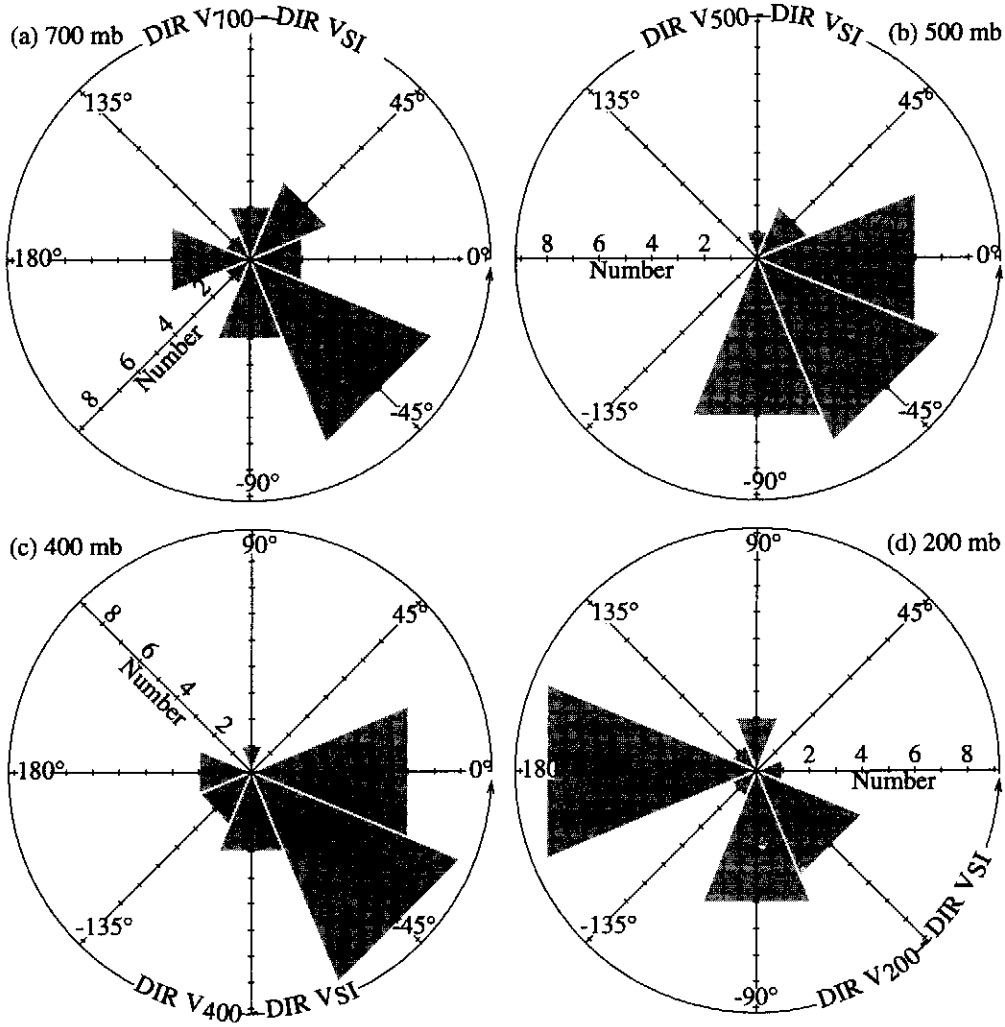

Figure 22. As Fig. 5 but a comparison of NCEP large-scale winds and stratiform inflow ($\mathbf{V}_{SI}$) in an earth-relative sense at 700, 500, 400 and 200 mb.

From the conceptual models in Figs. 8 and 20 there are six possible combinations of vector airflow parameters that could be used in the comparison of convective cells and stratiform precipitation. Two of these combinations involve airflow parameters that share a common sense of slope ($\mathbf{V}_{USO}$ versus $\mathbf{V}_{UI}$ and $\mathbf{V}_{DO}$ versus $\mathbf{V}_{SI}$) and thus might be expected to exhibit some correlation with each other. There is no systematic relationship between the direction or magnitude of $\mathbf{V}_{C_{USO}}$ and $\mathbf{V}_{C_{UI}}$. If these airflow parameters were connected, considerable directional and magnitude changes must have occurred in the regions between where the observations were made. In contrast, $\mathbf{V}_{C_{DO}}$ and $\mathbf{V}_{C_{SI}}$ tend to flow in the same plane (co-planar), most frequently in the same direction; they are never orthogonal, and $|\mathbf{V}_{C_{SI}}|$ is almost always greater than $|\mathbf{V}_{C_{DO}}|$ (Fig. 24). If connected, $\mathbf{V}_{SI}$ must usually undergo a deceleration in the process of merging with $\mathbf{V}_{DO}$.

The other four combinations of vector airflow parameters do not show a strong relationship to each other. However, it is apparent from all of the comparisons that the

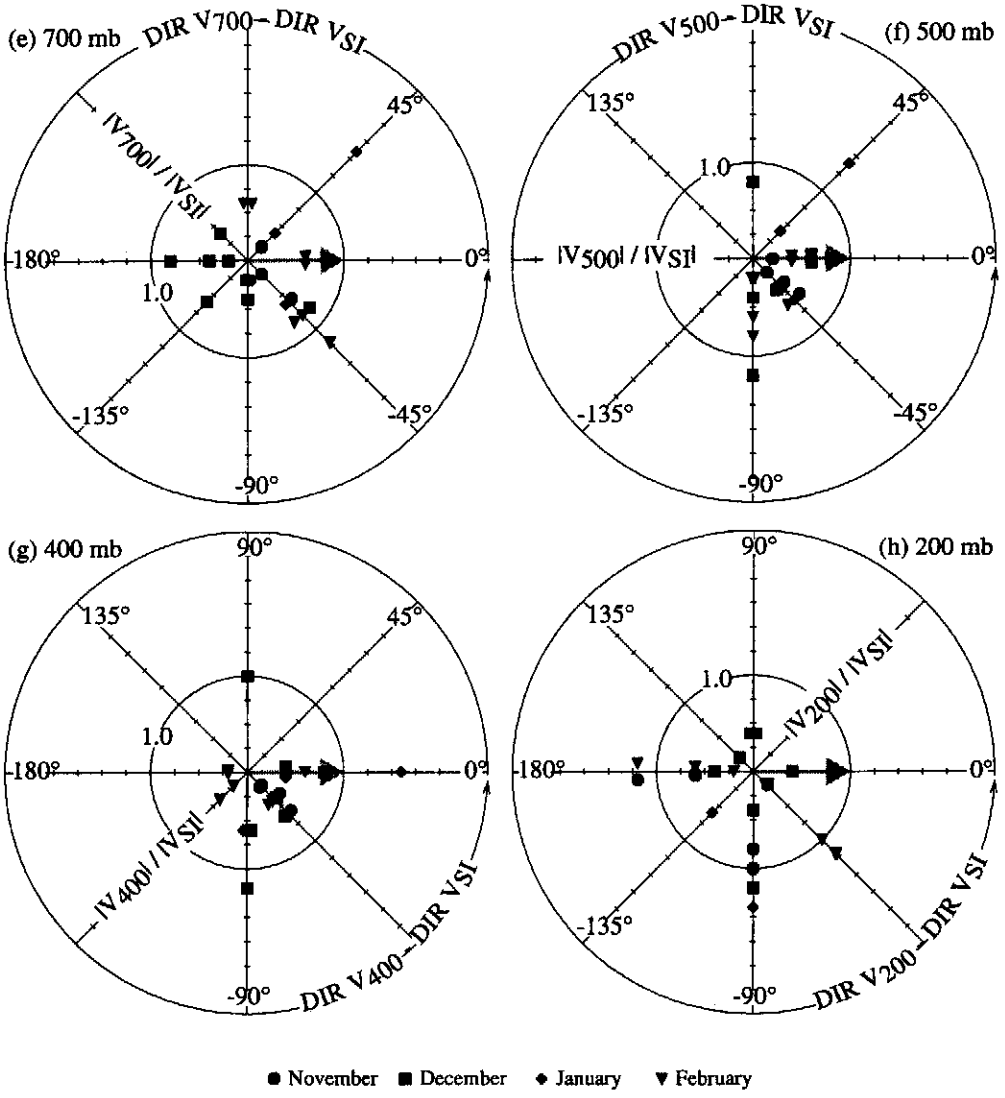

Figure 22. Continued.

stratiform inflow is the most dominant airflow parameter. Since it has larger magnitudes, extends over larger horizontal distances and maintains a more spatially continuous structure than the airflow parameters in convective cells, the stratiform inflow transports both mass and momentum in a manner that impacts the whole regions of the MPF. These results are consistent with Mapes and Houze (1992), who observed elevated jets that dominated the regions covered at low levels by boundary-layer cold pools in mesoscale convective systems over the oceanic warm pool near Australia. They suggested that these flow features were responsible for the lifting associated with developing convection. If the downdraught outflow is assumed to be connected to the stratiform inflow, our results are consistent with this hypothesis.

Lafore and Moncrieff (1989) and Weisman (1992) have demonstrated the importance of mid-level stratiform inflows in the momentum transport and convective development

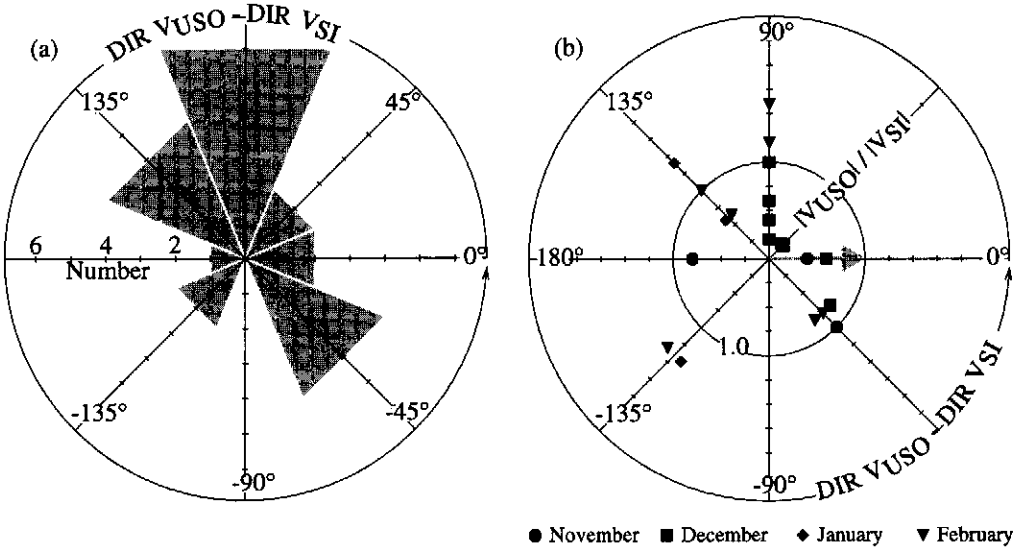

Figure 23. As Fig. 9 but a comparison of upper stratiform outflow (V_{USO}) and stratiform inflow (V_{SI}) in a cell-relative sense.

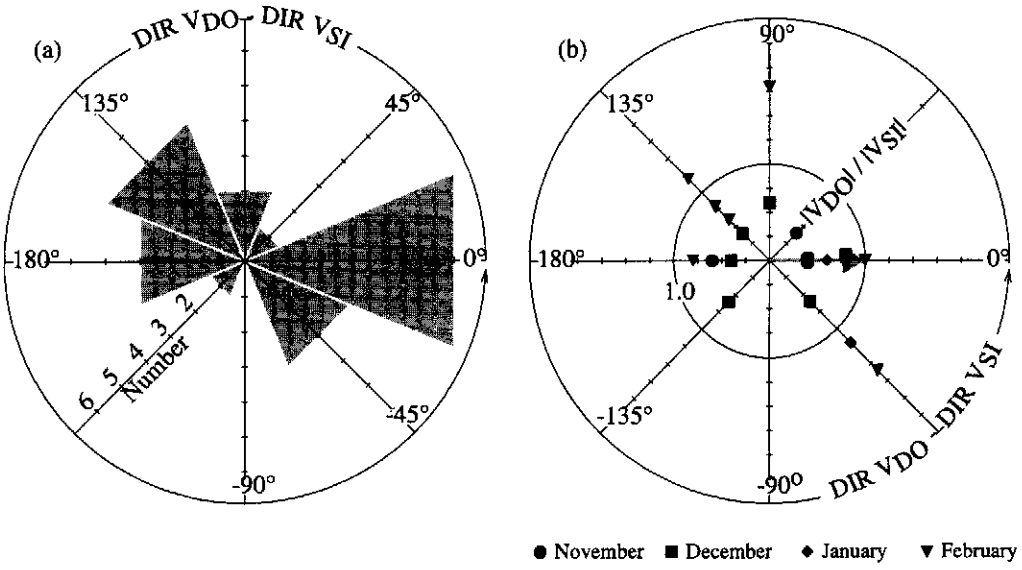

Figure 24. As Fig. 9 but a comparison of downdraught outflow (V_{DO}) and stratiform inflow (V_{SI}) in a cell-relative sense.

associated with numerically simulated MPFs. However, these studies did not conclude that the mid-level stratiform inflow dominated the formation and/or maintenance of the convective updraughts or downdraughts. The numerically simulated convection was, however, more spatially contiguous than the convection observed in COARE, and therefore could impact a larger portion of the MPF in a systematic way.

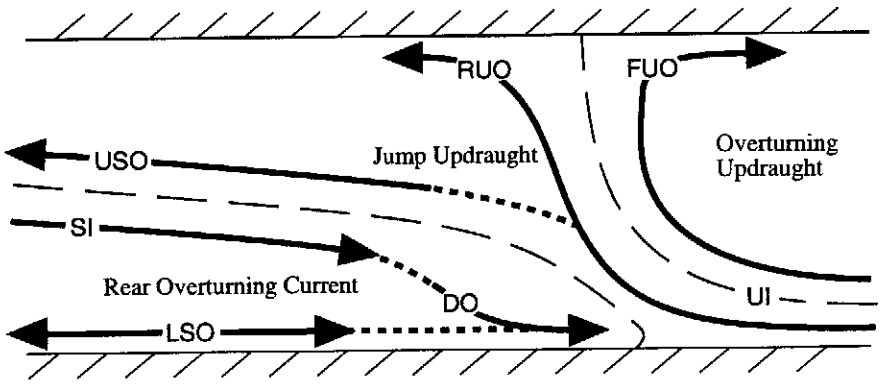

Figure 25. Modified schematic of the idealized flow fields used in the Moncrieff (1992) dynamic model of convective momentum transport based upon the results of this study. See text for further details.

7. Implications for parametrization of convective momentum transport

Convective momentum transport has been parametrized through the use of mass flux schemes that focus on ensembles of one-dimensional cumulus clouds (e.g. Schneider and Lindzen 1976; Tiedtke 1989). The Moncrieff (1992, hereafter M92) dynamic model of convective momentum transport (Fig. 1) has a greater degree of realism in that it is two-dimensional and incorporates horizontal pressure gradients and some aspects of mesoscale organization. It is most easily applied to mesoscale convective systems with a leading-line/trailing-stratiform precipitation structure (Houze *et al.* 1989, 1990; LeMone and Moncrieff 1994). The airborne radar observations analysed in this study provide an opportunity to test the wider applicability of M92 to the spectrum of precipitation warm-pool convection observed in COARE.

Figure 25 relates our results to those of M92. The intermittence of the aircraft sampling in time and space precluded a description of the complete MPF evolutionary cycle or simultaneous documentation of convective and stratiform regions. Short-dashed line segments in the figure speculate on the connections between the airflow structures from these two regions. The convective updraught inflow (UI), rear convective updraught outflow (RUO) and upper stratiform outflow (USO) collectively form an airflow structure that is consistent with M92's idealized 'jump updraught' (Fig. 1). Likewise, the convective updraught inflow and forward convective updraught outflow (FUO) combine to form a structure corresponding to M92's 'overturning updraught'. M92's 'rear overturning current' is less clear from our analysis, because the flow structure opposing the jump updraught exhibits characteristics of both a density current and a downdraught. The stratiform inflow (SI) resembles the upper branch of an overturning downdraught circulation. However, where it descends and connects with the downdraught outflow (DO), a density-current structure is formed. The lower stratiform outflow (LSO) is not well correlated with any of the other flow parameters, sometimes exhibiting a component of motion towards and sometimes away from the convective region. In making these comparisons, it should be noted that the idealized airflow in M92 is envisaged relative to a continuously propagating convective line. In contrast, the observed convection generally propagated discretely, making it difficult to determine a system-relative coordinate system.

The idealized airflow pattern in M92 (Fig. 1) is two-dimensional and conceptually simple. In contrast, the observations presented in this section suggest a more complex structure that is sometimes three-dimensional. Our adapted version of M92 in Fig. 25 is

rendered in a two-dimensional cross-section. This schematic should be considered more representative of air parcel streamlines than trajectories. The indicated airflow features had significant components in and out of the plane of the schematic, and it was difficult to define one dominant horizontal axis along which all the airflow could be seen. In addition, there was evidence of three-dimensionality, especially with respect to convective-cell flow parameters. Five of the MPFs contained multiple updraught-inflow/downdraught-outflow structures that were spatially discontinuous in terms of their directional characteristics (Table 4). Even the airflow in those MPFs with single updraught-inflow/downdraught-outflow structures was characterized by considerable spatial variability in magnitude and slope.

These results raise questions about the applicability of the conceptually simple version of the M92 model shown in Fig. 1 as a paradigm for momentum transport in the context of the highly complex structure of COARE mesoscale convective systems. One alternative might be to employ the vorticity-balance concepts described by Rotunno *et al.* (1988). In COARE, the vertical shear of the low- to mid-level horizontal wind is weak to moderate (Table 3) compared to the values used in their study. This suggests that the circulations generated by the convection in COARE are the primary means by which the mesoscale convective systems are organized. However, there are other factors to consider. The thermodynamic stratification associated with tropical environments is fundamentally different from the sounding representative of midlatitudes that was used by Rotunno *et al.* (1988). Although the vertically integrated values of buoyancy (i.e. convective available potential energy) in the two environments may be the same, the vertical distribution of buoyancy is usually different. In midlatitudes, buoyancy is greatest in the mid-troposphere and decreases near cloud base and cloud top. Conversely, in the tropics, buoyancy maintains similar values throughout the depth of the cloud. These differences have ramifications for the circulations generated by convection. In particular, cold pools generated by tropical convection (e.g. Houze 1977; Barnes and Garstang 1982; Parsons *et al.* 1994; Kingsmill and Houze 1999) tend to have smaller temperature deficits than those generated by midlatitude convection (e.g. Byers and Braham 1949; Fujita 1959; Goff 1976; Wakimoto 1982). Therefore, cold pools generated by tropical convection require less vertical shear to obtain an optimal vorticity balance, which suggests that shear may still be an important factor in the organization of tropical convection. However, the variability in convectively generated circulations is likely to exceed the variability in large-scale wind shear, which suggests that it may be necessary to understand more clearly how these circulations are generated to better parametrize momentum transport. Focusing attention on the most dominant circulation feature in COARE, the stratiform inflow, may be the key since it is well correlated with the large-scale winds and wind shear. In using this approach, many of the ideas inherent in the simplified M92 model may be found to apply in the more complex convective regime observed during COARE.

8. Conclusions

This analysis spanned the entire four-month period of TOGA-COARE, and examined 33 precipitation systems of various horizontal and vertical extents, within both the active and suppressed phases of the ISO. Convective structure and evolution was qualitatively consistent with the conceptual model developed by Leary and Houze (1979) for GATE convection. There was an overwhelming predominance of discretely propagating precipitation systems, and only an infrequent occurrence of continuously propagating squall lines with trailing stratiform precipitation (Table 3).

The airflow features in convective cells most commonly observed by Doppler radar were sloping updraught inflows and downdraught outflows separated by a nearly discontinuous interface. The updraught and downdraught channels sloped at various angles from the vertical and opposed each other from various horizontal directions (Figs. 6, 8 and 15; Table 4). Updraught inflows were variously shallow and deep, often originating above the boundary layer. The horizontal directions of both flow features were best related to the large-scale wind fields of the lowest 300 mb, especially at 850 mb (Figs. 10 and 11). In an earth-relative sense, the magnitudes of downdraught outflows were usually greater than those of updraught inflows (Fig. 9(b)). However, in a cell-relative sense they were more comparable (Fig. 14(b)). In either co-ordinate system, the horizontal directions of the convective-cell updraught inflow and downdraught outflow were usually offset from each other at $\sim|90°|$ (Figs. 9(a) and 14(a)).

In stratiform precipitation regions, the most common and robust airflow features observed by Doppler radar were gradually descending mid-level inflows, which usually manifested themselves at the base of an anvil overhang of radar echo but often extended into the interior of the precipitation system (Figs. 19 and 20; Table 5). These stratiform inflows most frequently originated between 5 and 10 km and descended about 3 km, although a few extended down to the surface (Fig. 21). They corresponded best in horizontal direction to the large-scale wind fields between 400 and 500 mb (Fig. 22). Stratiform inflow magnitudes were larger than the magnitudes associated with either the upper or lower stratiform outflows, especially in an earth-relative sense. The cell-relative directional difference between stratiform inflows and upper stratiform outflows was most frequently $\sim|90°|$ (Fig. 29(a)).

The relationship between flow parameters in convective cells and stratiform precipitation is complex. The mid-level stratiform region inflow pervades the whole precipitation area and is probably a key to the continued maintenance of very broad and deep precipitation areas. The convective downdraught outflow ($\mathbf{V}_{C_{DO}}$) and downward sloping inward penetrating mid-level stratiform inflow current ($\mathbf{V}_{C_{SI}}$) appear to connect. They behave somewhat two-dimensionally, as they tend to occur in the same vertical plane. $\mathbf{V}_{C_{SI}}$ appears to be slowed down by horizontal pressure gradients before it joins $\mathbf{V}_{C_{DO}}$ (Fig. 24).

The idealized airflow components used in the M92 dynamic model of convective momentum transport resemble the individual airflow features in the observed convective cells and stratiform precipitation. However, the Moncrieff model does not generally account for the structural complexity of the warm-pool convection. The mid-level stratiform inflow and its connection with convective downdraught outflow, however, may be the most important mesoscale circulation feature. It retains some degree of two-dimensionality and appears to have a systematic relationship to the large-scale ambient wind. These are characteristics that may turn out to be useful in the accurate parametrization of convective momentum transports.

ACKNOWLEDGEMENTS

The authors would like to thank Chris Bretherton, Peggy LeMone, Morris Weisman, Sandra Yuter and Ed Zipser for reviewing this manuscript. Stacy Brodzik, Shuyi Chen, Brian Mapes, Bradley Smull, Ming-Jen Yang and Sandra Yuter provided advice and comments during the course of this study. Candace Gudmundson edited the manuscript. Shannon O'Donnell performed the data processing tasks, including much of the airborne Doppler radar analysis. Gary Huitsing performed the cell-tracking analysis. Data were provided by NOAA (John Daugherty), the Atmospheric Technology Division of NCAR (Bob Rilling) and the University of California, Irvine (Carl Friehe, Sean Burns). This

research was supported by NOAA Cooperative Agreement NA67RJ0155. This is JISAO contribution number 448.

Appendix

List of symbols

Z_{TOP}	echo top
$\mathbf{V}_{PROP}$	cell propagation vector
$\mathbf{V}_{E_{UI}}$	earth-relative updraught inflow vector
$\mathbf{V}_{C_{UI}}$	cell-relative updraught inflow vector
$\mathbf{V}_{E_{DO}}$	earth-relative downdraught outflow vector
$\mathbf{V}_{C_{DO}}$	cell-relative downdraught outflow vector
$Z_{E_{UI}}$	earth-relative updraught inflow depth
$Z_{C_{UI}}$	cell-relative updraught inflow depth
$\Delta VR\|_{\Delta r=5\text{ km}}$	radial difference of radial velocity over a 5 km distance across the updraught–downdraught interface
$SLOPE_{UI}$	updraught inflow slope
VR_{FUO}	radial velocity of the updraught outflow exiting on the forward side of the cell
VR_{RUO}	radial velocity of the updraught outflow exiting on the rear side of the cell
ΔX_{UO}	horizontal distance separating VR_{FUO} and VR_{RUO}
α_{UO}	elevation angle from the aircraft to the location of updraught outflow
$Z_{E_{ORIG}}$	earth-relative origination height of the stratiform inflow
$Z_{E_{TERM}}$	earth-relative termination height of the stratiform inflow
ΔX_{SI}	horizontal extent of stratiform inflow
$SLOPE_{SI}$	stratiform inflow slope
ΔX_{ANVIL}	horizontal extent of anvil
$\mathbf{V}_{E_{SI}}$	earth-relative stratiform inflow vector
$\mathbf{V}_{C_{SI}}$	cell-relative stratiform inflow vector
$\mathbf{V}_{E_{USO}}$	earth-relative upper stratiform outflow vector
$\mathbf{V}_{C_{USO}}$	cell-relative upper stratiform outflow vector
$\mathbf{V}_{E_{LSO}}$	earth-relative lower stratiform outflow vector
$\mathbf{V}_{C_{LSO}}$	cell-relative lower stratiform outflow vector
$\Delta VR\|_{\Delta z=2.5\text{ km}}$	vertical shear of radial velocity over a 2.5 km distance above or below the stratiform inflow.

References

Alexander, G. D. and Young, G. S. 1992 The relationship between EMEX mesoscale precipitation feature properties and their environmental characteristics. *Mon. Weather Rev.*, **120**, 554–564

Barnes, G, M, and Garstang, M. 1982 Subcloud layer energetics of precipitating convection. *Mon. Weather Rev.*, **110**, 102–117

Barnes, G. M. and Sieckman, K. 1984 The environment of fast- and slow-moving tropical mesoscale convective cloud lines. *Mon. Weather Rev.*, **112**, 1782–1794

Battan, L. J. 1973 *Radar Observations of the Atmosphere.* University of Chicago Press, Chicago, USA

Byers, H. R. and Braham, R. R. Jr. 1949 *The Thunderstorm.* US Govt. Printing Office, Washington DC, USA

Cane, M. A. and Zebiak, S. E. 1985 A theory of El Niño and the southern oscillation. *Science*, **228**, 1085–1087

Chen, S. S, Houze, R. A. Jr. and Mapes, B. E. 1996 Multiscale variability of deep convection in relation to large-scale circulation in TOGA COARE. *J. Atmos. Sci.*, **53**, 1380–1409

Cheng, M-D. and Yanai, M. 1989 Effects of downdraughts and mesoscale convective organization on the heat and moisture budgets of tropical cloud clusters. Part III: Effects of mesoscale convective organization. *J. Atmos. Sci.*, **46**, 1566–1588

Chong, M., Amayenc P., Scialom G. and Testud, J. 1987 A tropical squall line observed during the COPT 81 experiment in west Africa. Part I: Kinematic structure inferred from dual-Doppler data. *Mon. Weather Rev.*, **115**, 670–694

Corbet, J., Mueller, C., Burghart, C., Gould, K. and Granger, G. 1994 Zeb: Software for geophysical data integration display, and management of diverse environmental datasets. *Bull. Amer. Meteorol. Soc.*, **75**, 783–792

Cressman, G. P. 1959 An operational objective analysis system. *Mon. Weather Rev.*, **87**, 367–374

Fujita, T. 1959 Precipitation and cold air production in mesoscale thunderstorm systems. *J. Meteorol.*, **16**, 454–466

Gamache, J. F. and Houze, R. A. Jr. 1982 Mesoscale air motions associated with a tropical squall line. *Mon. Weather Rev.*, **110**, 118–135

Godfrey, J. S., Houze, R. A. Jr., Johnson, R. H., Lukas, R., Redelsperger, J.-L., Sumi, A. and Weller, R. 1998 COARE: An interim report. *J. Geophys. Res.*, **103**, 14395–14450

Goff, R. C. 1976 Vertical structure of thunderstorm outflows. *Mon. Weather Rev.*, **104**, 1429–1440

Houze, R. A. Jr. 1977 Structure and dynamics of a tropical squall-line system observed during GATE. *Mon. Weather Rev.*, **105**, 1540–1567

1993 *Cloud Dynamics.* Academic Press, San Diego, USA

Houze, R. A. Jr. and Betts, A. K. 1981 Convection in GATE. *Rev. Geophys. Space Phys.*, **19**, 541–576

Houze, R. A. Jr., Rutledge, S. A., Biggerstaff, M. I. and Smull, B. F. 1989 Interpretation of Doppler weather-radar displays in midlatitude mesoscale convective systems. *Bull. Amer. Meteorol. Soc.*, **70**, 608–619

Houze, R. A. Jr., Smull, B. F. and Dodge, P. J. 1990 Mesoscale organization of springtime rainstorms in Oklahoma. *Mon. Weather Rev.*, **118**, 613–654

Johnson, R. H. and Nicholls, M. E. 1983 A composite analysis of the boundary layer accompanying a tropical squall line. *Mon. Weather Rev.*, **111**, 308–319

Jorgensen, D. P., LeMone, M. A. and Jou, B. J-D. 1991 Precipitation and kinematic structure of an oceanic mesoscale convective system. Part I: Convective line structure. *Mon. Weather Rev.*, **119**, 2608–2637

Jorgensen, D. P., Matejka, T. and DuGranrut, J. D. 1996 Multi-beam techniques for deriving wind fields from airborne Doppler radars. *Meteorol. Atmos. Phys.*, **59**, 83–104

Jorgensen, D. P., LeMone, M. A. and Trier, S. B. 1997 Structure and evolution of the 22 February 1993 TOGA COARE squall line: Aircraft observations of precipitation, circulation, and surface energy fluxes. *J. Atmos. Sci.*, **54**, 1961–1985

Keenan, T. D. and Carbone, R. E. 1992 A preliminary morphology of precipitation systems in tropical northern Australia. *Q. J. R. Meteorol. Soc.*, **118**, 283–326

Kingsmill, D. E. and Houze, R. A., Jr. 1999 Thermodynamic characteristics of air flowing into and out of precipitating convection over the west Pacific warm pool. *Q. J. R. Meteorol. Soc.*, **125**, 1209–1229

Klimowski, B. A. 1994 Initiation and development of rear inflow within the 28–29 June 1989 North Dakota mesoconvective system. *Mon. Weather Rev.*, **122**, 765–779

Lafore, J-P. and Moncrieff, M. W. 1989 A numerical investigation of the organization and interaction of the convective and stratiform regions of tropical squall lines. *J. Atmos. Sci.*, **46**, 521–544

Leary, C. A. and Houze, R. A. Jr. 1979 The structure and evolution of convection in a tropical cloud cluster. *J. Atmos. Sci.*, **36**, 437–457

LeMone, M. A. 1983 Momentum transport by a line of cumulonimbus. *J. Atmos. Sci.*, **40**, 1815–1834

LeMone, M. A. and Moncrieff, M. W. 1994 Momentum and mass transport by convective bands: Comparisons of highly idealized dynamical models to observations. *J. Atmos. Sci.*, **51**, 281–305

LeMone, M. A., Barnes, G. A. and Zipser, E. J. 1984a Momentum flux by lines of cumulonimbus over the tropical oceans. *J. Atmos. Sci.*, **41**, 1914–1932

LeMone, M. A., Barnes, G. A., Szoke, E. J. and Zipser, E. J. 1984b The tilt of the leading edge of mesoscale tropical convective lines. *Mon. Weather Rev.*, **112**, 510–519

Liu, C. and Moncrieff, M. W. 1996 Mass and momentum transports by organized convection: Effects of shear and buoyancy. *J. Atmos. Sci.*, **53**, 964–979

Ludlam, F. H. 1963 Severe local storms: a review. Pp. 1–30 in *Meteorological Monograph*, **5**, American Meteorological Society, Boston, USA

Madden, R. and Julian, P.	1972	Detection of a 40–50 day oscillation in the tropical Pacific. *J. Atmos. Sci.*, **29**, 702–708
Mapes, B. E. and Houze, R. A. Jr.	1992	An integrated review of the 1987 Australian monsoon and its mesoscale convective systems. I: Horizontal structure. *Q. J. R. Meteorol. Soc.*, **118**, 927–963
	1993	Cloud clusters and superclusters over the oceanic warm pool. *Mon. Weather Rev.*, **121**, 1398–1415
Martin, D. W. and Schreiner, A. J.	1981	Characteristics of West African and East Atlantic cloud clusters: A survey of GATE. *Mon. Weather Rev.*, **109**, 1671–1688
Mohr, C. G., Miller, L. J., Vaughan, R. L. and Frank, H. W.	1986	The merger of mesoscale data sets into a common Cartesian format for efficient and systematic analyses. *J. Atmos. Oceanic Technol.*, **3**, 144–161
Moncrieff, M. W.	1978	The dynamical structure of two-dimensional steady convection in constant vertical shear. *Q. J. R. Meteorol. Soc.*, **104**, 543–567
	1981	A theory of organized steady convection and its transport properties. *Q. J. R. Meteorol. Soc.*, **107**, 29–50
	1992	Organized convective systems: Archetypal dynamical models, mass and momentum flux theory, and parametrization. *Q. J. R. Meteorol. Soc.*, **118**, 819–850
Newton, C. W.	1963	Dynamics of severe convective storms. Pp. 33–58 in *Meteorological Monograph*, **5**, American Meteorological Society, Boston, USA
Oye, R. and Carbone, R.	1981	'Interactive Doppler editing software'. Pp. 683–689 in preprints of 20th conference on radar meteorology, American Meteorological Society, Boston, USA
Oye, R., Mueller, C. and Smith, S.	1995	'Software for radar translation, visualization, editing, and interpolation'. Pp. 359–361 in preprints, 27th conference on radar meteorology, American Meteorological Society, Boston, USA
Parsons, D., Dabberdt, W., Cole, H., Hock, T., Martin, C., Barrett, A-L., Miller, E., Spowart, M., Howard, M., Ecklund, W., Carter, D., Gage, K. and Wilson, J.	1994	The Integrated Sounding System: Descriptions and preliminary observations from TOGA COARE. *Bull. Am. Meteorol. Soc.*, **75**, 553–567
Riehl, H. and Malkus, J. S.	1958	On the heat balance in the equatorial trough zone. *Geophysica*, **6**, 503–538
Rotunno, R., Klemp, J. B. and Weisman, M. L.	1988	A theory for strong, long-lived squall lines. *J. Atmos. Sci.*, **45**, 463–485
Schneider, E. J. and Lindzen, R. S.	1976	A discussion of the parametrization of momentum exchange by cumulus convection. *J. Geophys. Res.*, **81**, 3158–3161
Shapiro, L. J. and Stevens, D. E.	1980	Parametrization of convective effects on the momentum and vorticity budgets of synoptic-scale Atlantic tropical waves. *Mon. Weather Rev.*, **108**, 1816–1826
Short, D. A., Kucera, P. A., Ferrier, B. S., Gerlach, J. C., Rutledge, S. A. and Thiele, O. W.	1997	Shipboard radar rainfall patterns within the TOGA COARE IFA. *Bull. Am. Meteorol. Soc.*, **78**, 2817–2836
Simpson, J. E.	1987	*Gravity currents: In the environment and the laboratory.* Cambridge University Press, Cambridge, UK
Smull, B. F. and Houze, R. A. Jr.	1987	Rear inflow in squall lines with trailing stratiform precipitation. *Mon. Weather Rev.*, **115**, 2869–2889
Thorpe, A. J., Miller, M. J. and Moncrieff, M. W.	1982	Two-dimensional convection in nonconstant shear: a model of mid-latitude squall lines. *Q. J. R. Meteorol. Soc.*, **108**, 739–762
Tiedtke, M.	1989	A comprehensive mass flux scheme for cumulus parametrization in large-scale models. *Mon. Weather Rev.*, **117**, 1779–1800
Ulanski, S. L., Hadlock, R. K. and Garstang, M.	1973	The role of convection in surface property and velocity fluctuations. *Boundary-Layer Meteorol.*, **6**, 183–195
Wakimoto, R. M.	1982	The life cycle of thunderstorm gust fronts as viewed with Doppler radar and rawinsonde data. *Mon. Weather Rev.*, **110**, 1060–1082
Webster, P. J.	1994	The role of hydrological processes in ocean–atmosphere interactions. *Rev. Geophys.*, **32**, 427–475
Webster, P. J. and Lukas, R.	1992	TOGA COARE: The coupled ocean–atmosphere response experiment. *Bull. Am. Meteorol. Soc.*, **73**, 1377–1416

Weisman, M. L. 1992 The role of convectively generated rear-inflow jets in the evolution of long-lived mesoconvective systems. *J. Atmos. Sci.*, **49**, 1826–1847

Williams, M. and Houze, R. A. Jr. 1987 Satellite-observed characteristics of winter monsoon cloud clusters. *Mon. Weather Rev.*, **115**, 505–519

Young, G. S., Perugini, S. M. and Fairall, C. W. 1995 Convective wakes in the equatorial western Pacific during TOGA. *Mon. Weather Rev.*, **123**, 110–123

Yuter, S. E., Houze, R. A. Jr., Smull, B. F., Marks, F. D. Jr., Daugherty, J. R. and Brodzik, S. R. 1995 TOGA COARE aircraft mission summary images: An electronic atlas. *Bull. Am. Meteor. Soc.*, **76**, 319–328

Zipser, E. J. 1969 The role of organized unsaturated convective downdraughts in the structure and rapid decay of an equatorial disturbance. *J. Appl. Meteorol.*, **8**, 799–814

Zipser, E. J., Meitin, R. J. and LeMone, M. A. 1981 Mesoscale motion fields associated with a slowly moving GATE convective band. *J. Atmos. Sci.*, **38**, 1725–1750